Ecofriendly High NIR Reflectance Ceramic Pigments Based on Rare Earths Compared with Classical Chromophores Prepared by DPC Method

Guillermo Monrós *, **José A. Badenes and Mario Llusar**

Department of Inorganic and Organic Chemistry, Jaume I University, Av. de Vicent Sos Baynat, s/n, 12071 Castellón, Spain
* Correspondence: monros@uji.es

Abstract: A high NIR reflectance ceramic pigments palette based on rare earths except black (La,Li-SrCuSi$_4$O$_{10}$ blue wesselsite, Pr-CeO$_2$ red-brown cerianite, Mo-Y$_2$Ce$_2$O$_7$ yellow cerate, Sr$_4$Mn$_2$CuO$_9$ black hexagonal perovskite) was compared with the coolest traditional pigments palette prepared by dry powder coating (DPC) to obtain "core-shell" pigments (Co-willemite blue, Cr-franklinite brown, Ni,Sb-rutile yellow, Co,Cr-spinel black). Adding CaCO$_3$ as a binder, normalized NIR reflectance at L* = 85, 55 and 30 was compared for yellow, brown and blue-black powders, respectively. Rare earths lack intense absorption bands in the NIR range and therefore its pigments show higher NIR reflectance, but normalized measurements show smaller differences and even have an inverse result for blue pigments. The pigmenting capacity and stability study in different media show that the stability of cool rare earth pigments is lower than that of DPC classical pigments, except in the case of the red-brown Pr-cerianite pigment.

Keywords: cool pigment; rare earth; normalized reflectance; DPC method; glazes

1. Introduction

The so-called eco-friendly cool pigments show high reflectance in the NIR region of the spectrum (700–2500 nm). The Dry Colour Manufacturers Association (DCMA) classifies pigments into three categories [1,2].

- *Category A* deals with pigments suspended in glass matrixes which require the highest degree of heat stability and chemical resistance to withstand the attack of molten glass.
- *Category B* deals with pigments suspended in plastics and other polymers, which require only moderate heat stability.
- *Category C* deals with pigments suspended in liquid vehicles, which require little, or no heat stability.

Colour is a subjective perception due to the sensitivity of the cone photoreceptors in the human eye to light (L long cones sensible to red colour, M middle to green and S short to blue light). There are different methods for an "objective" measurement of colour, such as the one developed by CIE (Comission International de l'Eclairage) [3]. The Colour Matching Functions (CMF), such as RGB or XYZ CIE models, deal with the accurate reproducibility of colour. On the other hand, Colour Appearance Models (CAM) try to evaluate the color with more intuitive parameters to human perception. They use parameters such as hue, saturation and brightness.

The CIEL*a*b* [3] colour space is referred to as standard lighting (e.g., D65) and an observer's field of view (e.g., 10°) uses three parameters: L* measures the lightness (100 for white, 0 for black) and a* and b* the colour parameters (−a* is the green axis, +a* the red axis, −b* the blue axis and +b* the yellow). The CIEL*C*h colour space correlates well with the colour perception of the human eye, and it has the same diagram as the L*a*b* colour

space but uses cylindrical coordinates instead of rectangular coordinates. In this colour space, L* indicates lightness such as in the CIEL*a*b* model, C* represents chroma, and h* is the hue angle. The value of chroma C* is the distance from the lightness axis (L*) and starts at 0 in the centre. Hue angle starts at the +a* axis and is expressed in degrees (e.g., 0° is red +a* axis, 90° yellow +b*, 180° green -a* and 270° is blue -b* axis). The values of C* and h* can be estimated from a* and b* parameters by the Equations (1) and (2), respectively:

$$C^* = (a^2 + b^2)^{1/2} \tag{1}$$

$$h^* = \arctan (b^*/a^*) \tag{2}$$

Colour systems based on hue, lightness and relative chroma first appeared in the early 19th century, but the key concept of absolute chroma was devised by the American artist Albert Munsell [4]. Lightness is associated with the range from black to white, and chroma or colour strength refers to the visual difference from a grey of the same value of lightness. As shown Figure 1, the chroma attainable for a given hue depends of the lightness [4,5]; the maximum chroma is obtained when Lightness L* (measured by the L*a*b* method) is high for yellow, cyan and green (L* = 80–90, 75–85 and 70–80 range respectively), middle for magenta and red (L* = 50–60, 45–55 respectively) and low for blue (25–35) shades.
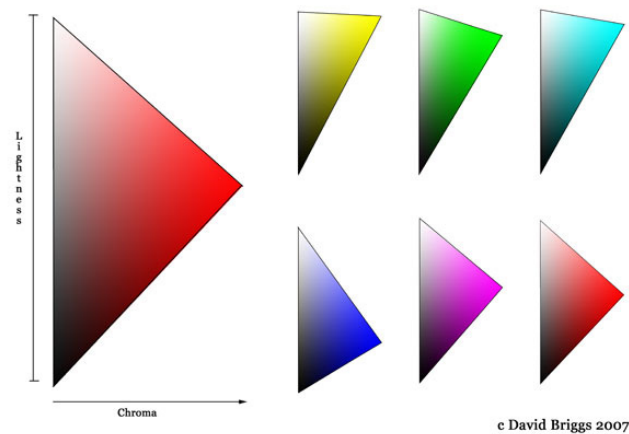
(**a**)
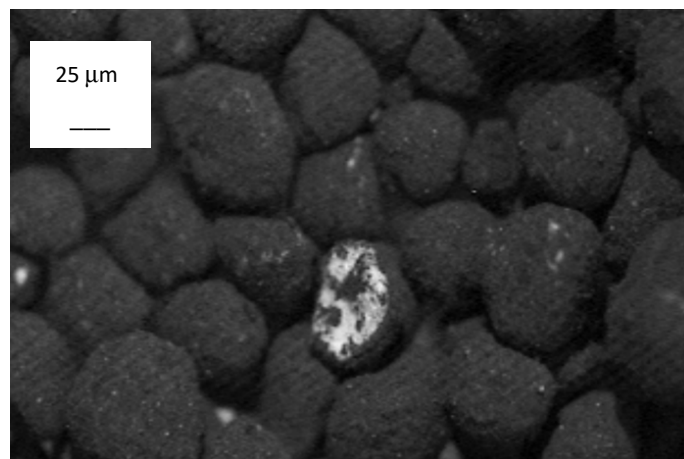
(**b**)

Figure 1. (**a**) Diagram of all possible RGB colours of a single hue angle, showing variations in the range of possible chroma with lightness. Reprinted with permission from Ref. [5], 2007. (**b**) Particles rejected on 60 μm sieve of the black pigment $0.1Co_3O_4.0.1Cr_2O_3@TiO_2$ obtained by dry powder coating (DPC).

Finally, Colour Difference Models (CDM) quantify how different two colours look from each other. One of these models is the CMC tolerance system based on CIELCh and provides better agreement between visual assessment and measured colour difference. CMC tolerance was developed by the Colour Measurement Committee (CMC) of the Society of Dyers and Colourists in Great Britain and became public domain in 1988. The tolerance ΔE^*_{CMC} for visual assessment between two colours is a 3-dimensional ellipsoid with axes corresponding to hue (Δh^*), chroma (ΔC^*) and lightness (ΔL^*) that is larger for chromatic colours (high $C^* > 10$). The CMC tolerance system is specified in the ISO International Standard 105-J03 (part J03: calculation of colour differences) [6] but other standards consider the tolerance of ΔE^* based on L*a*b* parameters:

$$\Delta E^* = \sqrt{\Delta L*^2 + \Delta a*^2 + \Delta b*^2}$$

(3)

ISO 12642-2 5 (referred to graphic technology to characterize the 4-color printing process) considers a difference $\Delta E^* > 5$ unacceptable. Instead, the International Standard ISO 10545-16 for ceramic tiles establishes a limit of $\Delta E^* < 0.75$ in part 16, concerning the determination of small colour differences between plain coloured ceramic tiles, which are designed to be of uniform and consistent colour.

1.1. Cool Pigments

As described above, cool pigments show high reflectance in the NIR range (750–2500 nm). When light falls on an object, both diffuse and specular reflections operate simultaneously. Diffuse reflection is considered to result from subsurface scattering; that is, light enters a surface layer, is scattered multiple times, and then exits in a random direction [7]. The spectrometers for collection of UV-Vis-NIR diffuse reflectance spectra give the data in absorbance using arbitrary units (A) or in reflectance (R) using the Kubelka–Munk model. The Kubelka–Munk (K-M) [8] transform of the measured diffuse reflectance is approximately proportional to the absorption, and hence to the concentration of absorbent species which absorbs light associated to charge transfer and d-d transitions of metal ions in lattice environments or also to stretching and deformation modes of functional groups (vibrations of supported species) [9].

Several physical parameters should be considered to achieve cool pigments [2]:

(a) Absence of absorbent ions in the NIR range (700–2500 nm.): e.g., Co^{2+} in a tetrahedral environment shows absorbance in the 1200–1600 nm (associated to the d-d transitions bands $^4A_2(F) \rightarrow {}^4T_1(F)$ at 1400 nm and $^4A_2(F) \rightarrow {}^4T_2(F)$ at 1600 nm), avoiding NIR reflectance in this NIR range, but an alternative for the blue colour in glazes is complicated [10].

(b) Therefore, a good cool pigment shows semiconductor behaviour with high band gap: e.g., TiO_2 (2.4 eV for anatase polymorph) or CdS, ZnO and $SrTiO_3$ (3.4 eV). They show intense charge transfer bands located at the UV region that block UV radiation, which provides protection to the organic binders.

(c) High thermal emittance. A good cool pigment shows the ability to release heat that it has absorbed and then its temperature decreases [11]. The emittance index of solids is high (e.g., ceramics 0.9, asphalt 0.88), but it is low for conductive metals (e.g., Ag 0.02, Al 0.03, Cu 0.04).

However, obviously, a pigment must show a high pigmentation performance when dispersed in the matrices (polymers, glass, ceramics . . .). To enable high dyeability, two parameters are critical [2]:

(a) High refractive index that allows for achieving high scattering efficiency of light when the pigment is added to a matrix with a very different refractive index. The scattering efficiency increases with the difference of the refractive index pigment-medium. For example, TiO_2 (anatase and rutile polymorphs) shows a high refractive index (2.55 and 2.73 respectively), therefore, the pigments based on rutile structure such as the yellow-orange of Cr-Sb rutile or yellow of Ni-Sb rutile are two of the best classical cool pigments. Related pigments such as Cr-pseudobrookite (Cr-Fe_2TiO_5) [12], Cr-armalcolite (Cr-($MgFe_2Ti_3O_5$) [13] or Ni-geikielite (Ni-$MgTiO_3$) [14] based on titanates also show high NIR reflectance.

(b) For an efficient scattering efficiency of light, the particle size should be about half the wavelength of the light; for NIR light (700–2500 nm), the particle diameter should be between 350–1250 nm. The particle shape and packing status are other important factors, in addition to the particle size. It is important to note that in ceramic applications, the particle size should be the minimum to avoid the attack of the media (glazes or ceramic stoneware); its size is between 0.1–5 µm and small particles can be dissolved by the melting glazes, decreasing the tinting strength of the pigment, and big particles decrease the density of the colour centres with the same result.

Opacity or hiding power of paints is the ability to hide the surface of an object. Opacity is dependent of the following characteristics: absence of absorbance bands in the NIR range, high scattering associated with the high miss-match between the refractive index of pigment and medium and an adequate particle size of the opacifier pigment. Moreover, the opacity increases with the thickness of the coating and, thus, the thickness should be similar when comparing the reflectance of coatings. Therefore, a cool pigment, that has high NIR transmittance, will require a NIR-reflective background (typically white or metallic) to produce an NIR-reflecting coating and the nature of the background of the coating modifies the reflectance of the coating; e.g., as 7% of the volume in alkyd paint, the nickel titanate yellow pigment changes from total solar reflectance R = 77–85% over a white background to 42–64% over a black background [15].

The total solar reflectance R, the solar reflectance in the NIR range R_{NIR} or the solar reflectance in the Vis range are evaluated from UV-Vis-NIR spectra through the diffuse reflectance technique, as the integral of the measured spectral reflectance and the solar irradiance divided by the integral of the solar irradiance is in the range of 350 to 2500 nm for R, 700 to 2500 nm for R_{NIR} or 350–700 nm for R_{Vis} as in the Equation (4):

$$R = \frac{\int_{350}^{2500} r(\lambda)i(\lambda)d\lambda}{\int_{350}^{2500} i(\lambda)d\lambda} \qquad (4)$$

where $r(\lambda)$ is the spectral reflectance (Wm^{-2}) measured by UV-Vis-NIR spectroscopy and $i(\lambda)$ is the standard solar irradiation ($Wm^{-2} nm^{-1}$) according to the American Society for Testing and Materials (ASTM) Standard G173-03.

Buildings contribute to climate change with their greenhouse gas emissions (e.g., 30% of the total emitted by the U.S.) associated with their primary energy consumption (36% of the total in the U.S.). For this reason, minimization strategies have been undertaken through different certification systems such as BREEM, or the Building Research Establishment Environmental Assessment Method, the oldest green building rating system (1990), Miljöbyggnad, or Environmental Building in English, created by the Sweden Green Building Council in 2010 or the Leadership in Energy and Environmental Design (LEED) certification, promoted by the U.S. Green Building Council. These "Green Building Rating Systems" (GBRS) analyse the sustainability of buildings considering several factors associated with their design and construction, such as the content of recycled material and the heat island effect (HIE). Determination of the Solar Reflectance Index (SRI) for opaque materials (wall, roof and floor) reveals the ability of a surface to reflect solar radiation and to emit thermal radiation, reducing the increase in temperature caused by the incidence of solar radiation on the surface aids of all GBRS. As described above, the SRI of a specific

surface depends on the solar reflectance and thermal emittance of the material, but also of the solar flux, the convection coefficient, the air temperature and the sky temperature (ASTM E1980 2011). For roof tiles for buildings, the SRI value required is dependent on the slope of the roof (SRI $\geq$ 39 for steep slope; SRI $\geq$ 82 for low slope).

1.2. Rare Earths and Cool Pigments

Following Dieke [16], the trivalent rare earth ions, $[Xe]4f^n$, involves the activity of internal f electrons, strongly protected by 5s and 5p electrons. Because of the shielding effect of the outer 5s and 5p shell electrons, the crystal-field interaction with inner 4f electrons is weak and can be treated as a perturbation (Stark effect) of the free-ion states. Accordingly, the energies of the corresponding levels of $4f^n$ configuration are only weakly sensitive to the type of the crystal host. Therefore, the resulting crystalline field caused by their interaction with neighbouring ions is very low, and usually optical spectra of lanthanide compounds present weak and profuse bands. On the other hand, the 5d electrons are not effectively shielded by other electrons, and the crystal field influence on the energy levels of $4f^{n-1}5d^1$ electronic configuration is strong. Accordingly, crystal field splitting of 5d levels is large and the energies of levels within $4f^{n-1}5d^1$ electronic configuration can strongly differ for different crystal hosts [16].

The classical complex inorganic pigments based on mixed metal oxides are based on transition metals and the mechanism of colour is associated with its broad and intense absorption bands due to d-d transitions that fall within the visible range: however, transition metals such as Co, Cr or Ni are toxic, therefore, new inorganic pigments that reflect the NIR range and are less hazardous for the environment need to be developed [17,18].

In the case of rare earth-based pigments, the mechanism of the colour is associated with the shift of the charge transfer band of a semiconductor to higher wavelengths, by introducing an additional electronic level through doping with a chromophore rare earth ion. For example, CeO_2 crystallizes in the fluorite structure, where FCC packed Ce^{4+} ions are surrounded by eight oxide ions, occupying alternate centres of tetrahedral cavities in the FCC lattice. The 4f valence shell of $Ce^{4+}([Xe])$ in cerianite is empty, and that of O^{2-} $([He]2s^2\,2p^6)$ is full; adjacent Ce^{4+} ions are virtually in contact in the fluorite lattice and, as a result, 4f orbitals overlap in a cationic conduction band; similarly, overlap of 2p orbitals of oxygen ions gives an anionic valence band. The band gap between the anionic band and the cationic band is 2.76 eV [18]. Pr^{4+} doping into cerianite introduces an additional conduction band and its associated charge transference band absorbs from 600 nm (band gap 2.0 eV), inducing a brown colon; since all wavelengths above 570 nm are reflected, except the weak and sharp absorption due to 4f transitions, $Pr^{4+}:CeO_2$ is a good NIR reflector material.

Recently, the industrial utilization of lanthanides has increased rapidly because of their low toxicity [18,19]; consequently, a large number of rare earths based on NIR reflective pigments have been proposed as an alternative to traditional pigments:

(a) For blue pigments, Smith et al. [20,21] synthesized by ceramic route at 1200 °C the solid solution Mn-YInO$_3$ with perovskite structure (YIn$_{0.8}$Mn$_{0.2}$O$_3$ powder shows L*a*b* = 34.1/11.7/$-$44.4 and R = 34%, and 20% in vinyl paint 77.9/$-$2.9/$-$19.3 with R$_{NIR}$ = 62%). Sheethu et al. and Zhang et al. [22,23] describe blue pigments based on the solid solutions of rare earths in wesselsite SrCuSi$_4$O$_{10}$ (Sr$_{0.3}$La$_{0.7}$Cu$_{0.3}$Li$_{0.7}$Si$_4$O$_{10}$ powder, which shows L*a*b* = 49.6/10.4/$-$51.7 and R$_{NIR}$ = 66% obtained by the ceramic route at 950 °C/16 h, whereas Sr$_{0.8}$Eu$_{0.2}$Cu$_{0.3}$Si$_4$O$_{10}$ shows L*a*b* = 46.6/$-$4.6/$-$28.1 and R$_{NIR}$ = 72.3 synthesized by the citrate route at 900 °C/2 h).

(b) For magenta-brown shades, García et al. and Llusar et al. [18,19] describe the application of brown-red pigments based on Ce$_{1-x}$M$_x$O$_2$ solid solutions (M = Pr,Tb) showing R$_{NIR}$ = 80% for x = 0.05 in glazes. Vishnu et al. [24] report brown pigments by solid state reaction at 1500 °C/18 h based on the solid solution Pr-Y$_2$Ce$_2$O$_7$ with fluorite structure (Y$_2$Ce$_{1.7}$Pr$_{0.3}$O$_7$ powder shows L*a*b* = 32.6/18.1/12 and R$_{NIR}$ = 58%) and yellow pigments from Mo-Y$_2$Ce$_2$O$_7$ solid solutions (Y$_2$Ce$_{1.5}$Mo$_{0.5}$O$_7$ powder shows L*a*b* = 90.2/$-$4.5/62.4 and R$_{NIR}$ = 81%); later, Raj et al. [25] report a brown pigment

doping with Tb as the same structure. Jovani et al. [26] report a brown pigment based on $Y_{2-x}Tb_xZr_{2-y}Fe_yO_{7-\delta}$ (L*a*b* = 64/34/33 for 4 wt.% addition in a conventional frit of powder x = 0.35).

(c) For yellow pigments, Gargori et al. [27] report the preparation of a yellow pigment based on the codoped V^{5+},Ca^{2+}-$Y_2Sn_2O_7$ pyrochlore ($Ca_xY_{2-x}V_ySn_{2-y}O_7$) solid solutions at 1200 °C/6 h (the powder x = y = 0.16 shows L*a*b*= 85.7/1.1/34 and 5 wt.% enamelled in a double firing frit at 1000 °C shows L*a*b* = 79.3/2.6/35 with R_{NIR} = 81%). Liu et al. [28] develop by citrate route at 700 °C/6 h high NIR reflectance yellow pigments based on Al-$LaFeO_3$ ($LaAl_xFe_{1-x}O_3$) perovskite solid solutions; at low x the colour is brown and at x > 0.7 it is yellow (L*a*b* = 71.2/2.8/10.0 with R_{NIR} = 57%). Although the authors do not evaluate the NIR reflectance, the $(Ca_{1-x-y}Eu_xZn_y)_2Al_2SiO_{7+\delta}$ ($0 \leq x \leq 0.15; 0 \leq y \leq 0.07$) solid solutions with gehlenite structure ($Ca_2Al_2SiO_7$) show high NIR reflectance, and $(Ca_{0.87}Eu_{0.10}Zn_{0.03})_2Al_2SiO_{7+\delta}$ pigment exhibited the most vivid yellow colour (L*a*b* = 74/0/76) [29]. The origin of the yellow colour is the 4f-5d transition of divalent Eu^{2+} ion, and codoping with Zn enhances the yellowness by increasing the Eu^{2+} amount in the samples. Schildhammer et al. report a yellow pigment based on $Yb_6Mo_2O_{15}$ crystallizing in a trigonal structure by ceramic method at 1350 °C/20 h with the colour coordinates L*a*b* = 88.7/6.6/55 and R_{NIR} = 94%. Colour variation from pale yellow to brick-red was realized by partial substitution of Yb^{3+} or Mo^{6+} with various metal ions [30].

(d) Obtaining black pigments based on rare earths as chromophores is very complicated given that the origin of the colour, as discussed above, is based on 4f-5d transitions or on the generation of additional charge transfer bands induced by entrance of rare earths ions in the network, because the absorptions associated with 4f transitions are sharp and weak. Thus, rare earth chromophores only absorb in the blue-green range producing yellow or brown colours; blues are due to traditional chromophores in the rare earth network such as Mn^{3+} in trigonal bipyramid [20,21], which could be obtained in other free-rare earth structures [31], or to weakly allowed bands associated to Cu^{2+} [22,23] that connect with ancient pigments such as the Egyptian Blue Family [32,33]. Therefore, to obtain a whole absorbent pigment of the visible range is virtually impossible using rare earths as chromophores, but there are black or dark brown pigments involving rare earth lattices: Gargori et al. describe a black pigment based on perovskite $CrNdO_3$, and a green pigment that turns into black when it is modified by fluorides [14], probably associated to the high concentration of vacancies introduced by the dopants [34] (adding 2 wt.% BaF_2 and 8 wt.% MgF_2 at 1100 °C/3 h the powder shows L*a*b* = 43.4/2.4/4.0 but low R_{NIR} = 4%). Likewise, the undoped $YInO_3$ shows a black colour although the authors [20,21] only measure the NIR reflectance of the Mn^{3+} doped blue pigment.

1.3. Dry Powder Coating (DPC) Method

Several of the published cool pigments are only evaluated in powder form and, sometimes, their lightness is outside Munsell's optimal chroma, resulting in pale colours [4]. In this work, a palette of pigments based on rare earths have been chosen. This palette along with a non-classical black pigment are synthesized and characterized as cool pigments. Likewise, a palette of classical pigments synthesized by a dry powder coating (DPC) method is compared with the rare earth palette. DPC methods produce "decorated" or "core-shell" pigments in which a core of high reflectance ceramic base (the core, e.g., TiO_2, ZnO) is coated by a shell of the pigment.

The DPC coating method has been utilized for producing special chemicals and ceramics under wet or dry conditions for improving its functionalities. In the dry method, a host of reflectance particles (1–500 μm, e.g., ZnO) are coated mechanically with a guest of chromophore particles (0.1–50 μm, e.g., Fe_2O_3 and Cr_2O_3) in order to improve wettability, solubility and other characteristics such as reactivity [35]. As the guest particles are so fine, the van der Waals interactions are sufficiently strong to keep them firmly attached to

the host particles. Thus, either a discrete or continuous coating of guest particles can be achieved depending on the choice of equipment or operating conditions such as processing period, mechanical action, weight fraction of guest to host particles and physical properties of the particles used [36]. This discrete or continuous coating of guest particles reacts when firing, giving a shell over the core of the host particles (e.g., Fe_2O_3 and Cr_2O_3, reacts over the coated ZnO particles to give franklinite Zn $(Cr,Fe)_2O_4$)).

Figure 1b shows the particles rejected on a 60 μm sieve of the black pigment $0.1Co_3O_4 \cdot 0.1Cr_2O_3@TiO_2$ obtained by the dry powder coating (DPC) procedure, fired at 1100 °C/3 h, which is discussed below, showing the "core-shell" feature of the pigment with a core of high reflectance base (in this case white TiO_2) coated by a layer of the pigment.

2. Materials and Methods

2.1. Samples Preparation

The cool pigments palette based on rare earths (except black) is integrated by the following pigments:

(a) Blue of La,Li doped $SrCuSi_4O_{10}$ wesselsite [22] (structure of gillespite $BaFe^{2+}Si_4O_{10}$, tetragonal, Space Group *P4/ncc* [33]). A total of 50 g of the composition $Sr_{0.3}La_{0.7}Cu_{0.3}Li_{0.7}Si_4O_{10}$ was prepared from carbonates ($SrCO_3$ and Li_2CO_3) and oxides (La_2O_3, CuO, quartz SiO_2).

(b) Red-brown of Pr-CeO$_2$ cerianite (fluorite structure, cubic, Space Group *Fm3m*) [18]. In total, 50 g of the composition $Ce_{0.95}Pr_{0.05}O_2$ was prepared from oxides (Pr_6O_{11}, CeO_2).

(c) Yellow of Mo-$Y_2Ce_2O_7$ yttrium cerate (fluorite structure, cubic, Space Group *Fm3m*) [24]. A total of 50 g of the composition $Y_2Ce_{1.5}Mo_{0.5}O_7$ was prepared from $(NH_4)_2MoO_4$ and oxides (Y_2O_3, CeO_2).

(d) Black-brown of $Sr_4Mn_2CuO_9$ (hexagonal perovskite, Space Group *P321*) [37]. The structure of this pigment consists of octahedra and trigonal prisms that form a chain structure by face-sharing. The Mn^{4+} ions occupy octahedral sites and Cu^{2+} ions randomly fill the centre of the square faces of the trigonal prisms. A total of 50 g of the composition $Sr_4Mn_2CuO_9$ were prepared from carbonates ($SrCO_3$) and oxides (MnO_2, CuO).

The coolest pigment palette based on traditional pigments with transition metals chromophores, optimized by dry powder coating (DPC), is integrated by the following pigments:

(a') Blue of Co-Zn_2SiO_4 willemite-decorated ZnO (trigonal, Space Group *R-3*) [38]. A total of 50 g of the composition $[Co_{0.6}Zn_{1.4}SiO_4] \cdot 0.2ZnO$ was prepared from oxides (Co_3O_4, ZnO, quartz SiO_2).

(b') Red-brown of Cr-$ZnFe_2O_4$ Franklinite-decorated ZnO (CPMA number 13-37-7, spinel, cubic, Space Group *Fd3m*) [39]. In total, 50 g of the composition $[ZnFe_{1.8}Cr_{0.2}O_4]$. ZnO was prepared from oxides (Cr_2O_3, Fe_2O_3 hematite, ZnO).

(c') Yellow of Ni,Sb-TiO_2-decorated TiO_2 (CPMA number 11-15-4, tetragonal, Space Group *P42/mnm*) [40]. A total of 50 g of the composition $[Ni_{0.25}Sb_{0.25}Ti_{0.5}O_2]$. TiO_2 was prepared from oxides (Sb_2O_3, TiO_2 anatase, NiO).

(d') Black-green of $Co(Cr_{2-x}Co_x)O_4$-decorated TiO_2 (spinel CPM number 13-29-2, cubic, Space Group *Fd3m*) [41,42]. In total, 50 g of the composition $[Co(Cr_{1.2}Co_{0.8})O_4]$. TiO_2 was prepared from oxides (Co_3O_4, Cr_2O_3, TiO_2 anatase).

Precursors, supplied by ALDRICH, with a particle size between 0.3–5 μm except the ZnO used as core in the DPC procedure with relatively high particle size (1–45 μm, ref. Zn526010), were mechanically homogenized in an electric grinder (20,000 rpm) for 5 min. The mixture was fired at the corresponding temperatures and soaking times: 950 °C/16 h (pigment a), 1400 °C/6 h (pigment b), 1500 °C/6 h (pigment c), 1000 °C/6 h (pigment d) and 1100 °C/3 h (pigments a', b', c' and d'). The fired powders were sieved using a 60 μm sieve.

2.2. Samples Characterization

X-ray Diffraction (XRD) was carried out on a Siemens D5000 diffractometer using Cu K_α radiation (10–70° 2θ range, scan rate 0.02° 2θ, 4 s per step and 40 kV and 20 mA conditions).

L*a*b* and C*h* colour parameters of glazed samples were measured following the CIE-L*a*b* ("Commission Internationale de l'Éclairage") colorimetric method[3] using a X-Rite SP60 spectrometer, with standard lighting D65 and 10° observer. With this method, L* is a measure of lightness (100 = white, 0 = black) and a* and b* of colour parameters (−a* = green, +a* = red, −b* = blue, +b* = yellow).

UV-Vis-NIR spectra of fired powder samples and also of the applications of the pigments samples were collected using a Jasco V670 spectrometer through diffuse reflectance technique, which gives data in absorbance using arbitrary units (A) or in reflectance units (R (%)) using the Kubelka–Munk transformation model. The optical reflectance spectra were scanned in the range of 350 to 2500 nm for optimized pigments, and the total solar reflectance R and the NIR solar reflectance R_{NIR} were obtained as discussed above (Equation (4)).

Microstructure characterization of powders was carried out by Scanning Electron Microscopy (SEM) using a JEOL 7001F electron microscope (following conventional preparation and imaging techniques). The chemical composition and homogeneity of the samples was determined by semi-quantitative elemental analysis with an EDX analyser (supplied by Oxford Indstruments, Abingdon, UK) attached to the microscope.

Band gap energy of semiconductors was calculated by Tauc plot using the UV-Vis-NIR spectra of the Kubelka–Munk model [30].

2.3. Application of Pigments

The colouring capacity of the pigments was studied in three matrices: (a) 10 wt.% in colourless alkyd paint, (b) 3 wt.% in a conventional lead-free double-firing frit of the SiO_2-CaO-ZnO system (1050 °C, widely employed for the double firing glazed tiles for wall cladding) and (c) 2 wt.% in porcelain powder (1190 °C).

3. Aims

In conclusion, cool pigments show high values of R and R_{NIR} along with high stability and colouring capacity in its applications, showing high chroma C* (except for black hues which tends to zero) and lightness L* should be enclosed within the range of Munsell's high chromaticity for the different hues (e.g., high for yellow (80–90), cyan (75–85) and green (70–80), middle for magenta (50–60) and red (45–55) and low for blue (25–35) and black (30-0) hues (see Figure 1a) [43]). Authors have associated the high reflectance or SRI (Solar Reflectance Index) with the lightness L* or Y factor. For instance, L. M. Schabbacha et al. analysed the thermal and optical properties related to the solar reflectance index in pigmented glazed ceramic roof tiles in Brazil [44]; the results show that most of the coloured glazed tiles did not meet the 2013 LEED requirement, that is, SRI ≥ 39 for roof tiles with a steep slope.

As said before, several of the published cool pigments are only evaluated in powder form and, sometimes, their lightness is outside Munsell's optimal chroma, resulting in pale colours [4]. In this work, a palette of pigments based on rare earths and a classic palette are synthesized and characterized as cool pigments at normalised L*. For a rigorous comparison of the cool performance of two pigments, its L* values should be the same, hence, the measurement of a normalized reflectance; e.g., R85 (R at L* = 85) for yellow and cyan hues, R75 for green, R55 for brown-magenta and R30 for blue and black hues is proposed. These evaluations can be obtained by gradual addition of the pigment to the matrices or using a binder (e.g., $CaCO_3$) in the case of powder. Calcite ($CaCO_3$), a cheaper and abundant high NIR reflectance white compound ($R_{Vis}/R_{NIR}/R$ = 80/60/70) [45], is mixed as a binder with the pigments in an electric grinder (20,000 rpm) for 5 min.

4. Results and Discussion

4.1. X-ray Diffraction (XRD) and SEM-EDX Characterization

The XRD patterns of the powders are shown in Figure 2, and the SEM images of powders (at low and high magnification) in Figure 3, whereas additional SEM images with their corresponding EDX mappings of powders are shown in Figure 4.
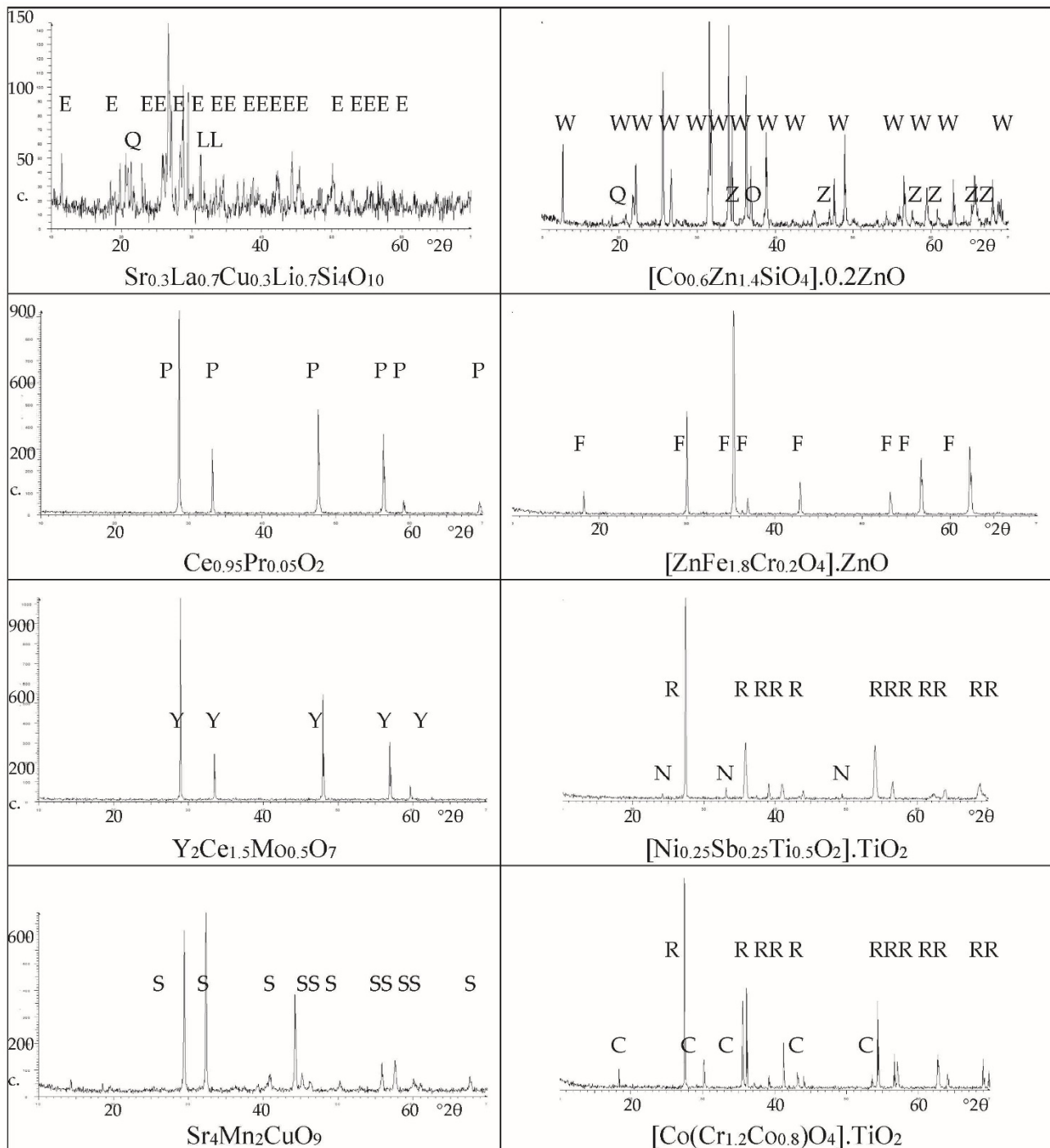
Figure 2. XRD patterns of powders. CRYSTALLYNE PHASES: E (wesselsite $SrCuSi_4O_{10}$), L (La_2O_3), W (willemite Zn_2SiO_4, Q (quartz), Z (ZnO), O (Co_3O_4), P (CeO_2) F (Franklinite $ZnFe_2O_4$), Y ($Y_2Ce_2O_7$), R (rutile), N ($NiTiO_3$), S ($Sr_4Mn_2CuO_9$) and C ($CoCr_2O_4$).
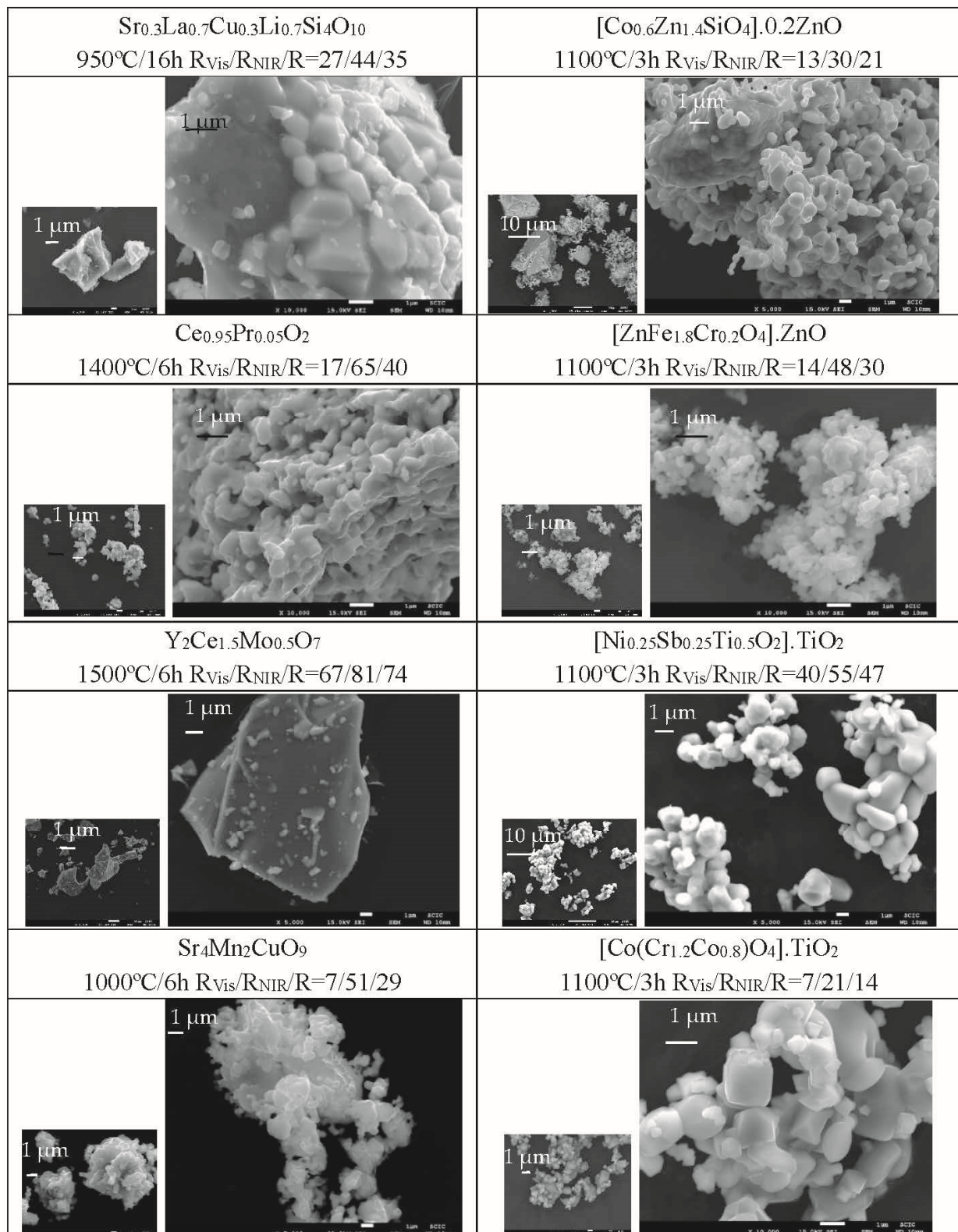
Figure 3. SEM images of powders of the both families of pigments.

Figure 4. *Cont.*

$Sr_4Mn_2CuO_9$ 1000°C/6h $R_{Vis}/R_{NIR}/R$=7/51/29	$[Co(Cr_{1.2}Co_{0.8})O_4].TiO_2$ 1100°C/3h $R_{Vis}/R_{NIR}/R$=7/21/14
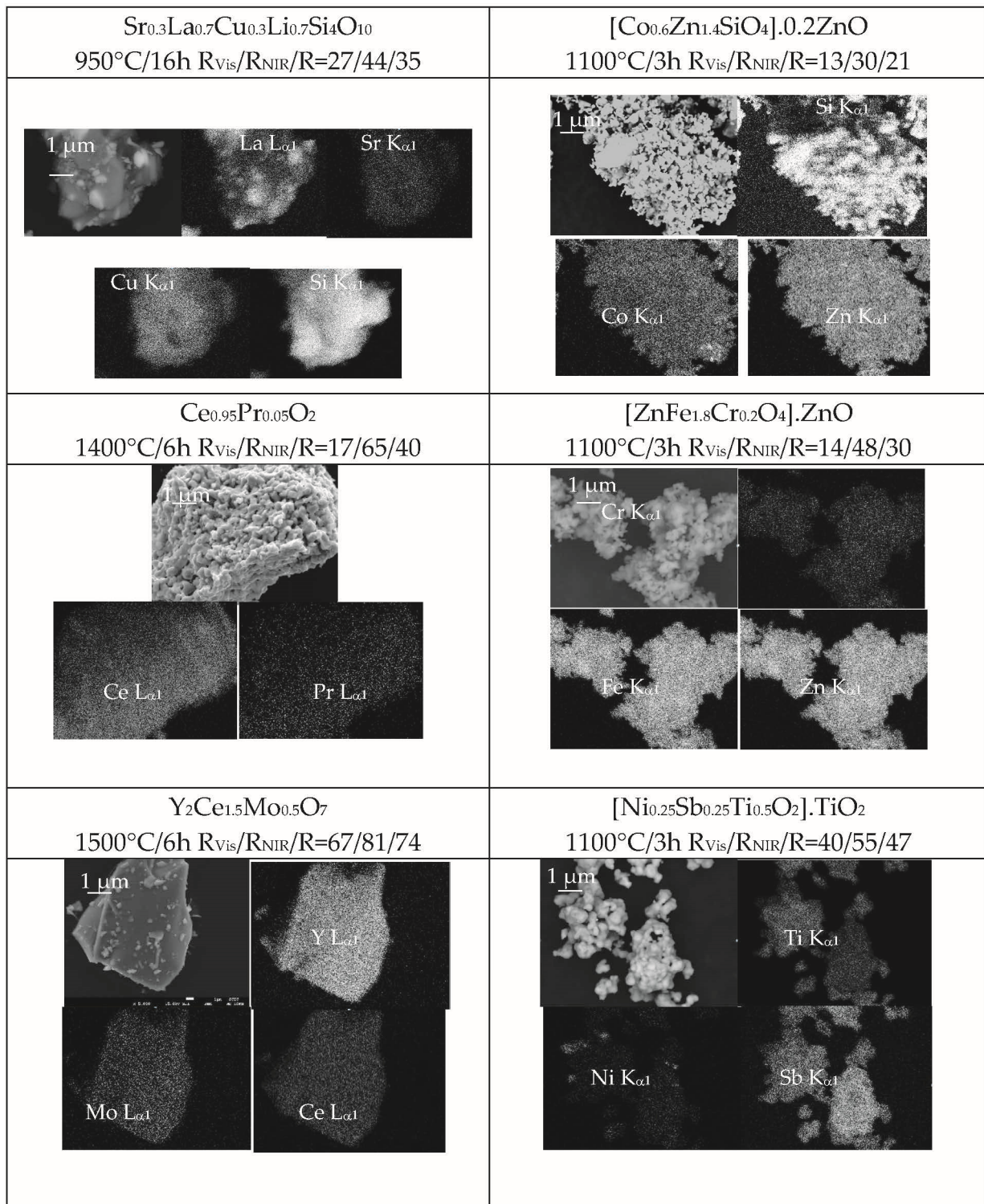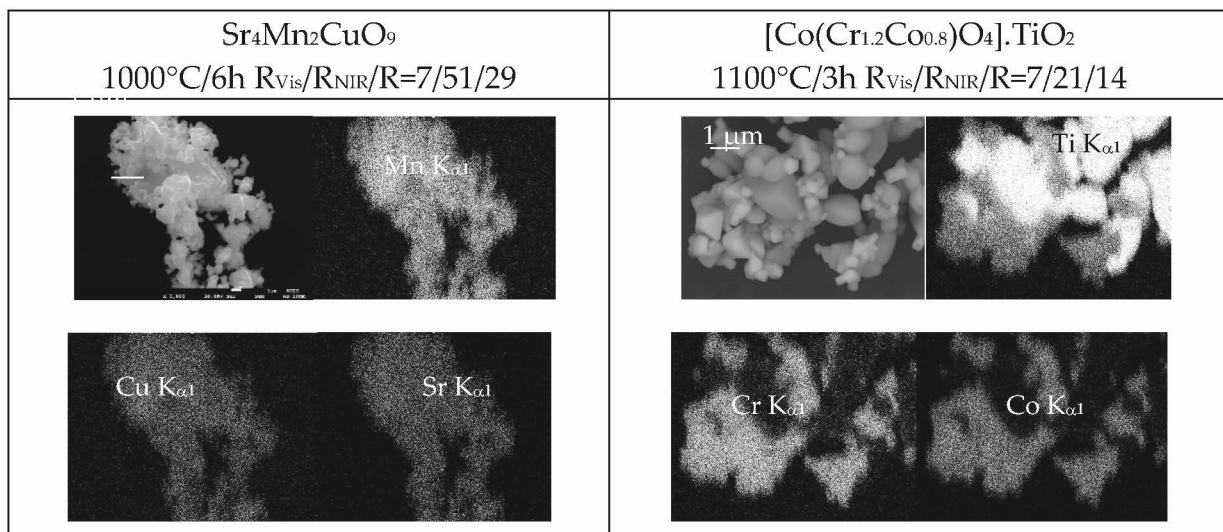
Figure 4. SEM and correlated EDX mapping of powders of the both families of pigments.

(a) In the case of blue pigments, XRD shows the crystallization of wesselsite $SrCuSi_4O_{10}$ (E in Figure 2) as the main crystalline phase, although several weak peaks associated to residual quartz (Q) and La_2O_3 (L) are detected. For the classical Co-willemite-decorated ZnO, willemite and ZnO are the main phases, but weak XRD peaks of unreacted quartz and Co_3O_4 are also detected. The SEM images (Figure 3) show that the La,Li-wesselsite blue powder presents aggregates of 10 µm of mean size highly sintered, and are sometimes decorated by little orthohedrons with particle sizes between 0.2–1 µm. The microstructure of Co-willemite blue pigment is homogeneous, showing aggregates between 5–25 µm integrated with fine spherical particles of around 1 µm of particle size. The SEM-EDX results in Figure 4 are in agreement with XRD observations: the La $L_{\alpha1}$ signal show the presence of unreacted lanthanum oxide in the La,Li-wesselsite blue powder, whereas unreacted quartz along with a little Co inhomogeneity are also detected in the mapping of the Co-willemite powder.

(b) Regarding red-brown pigments, cerianite (P) is the only crystalline phase detected for Pr-cerianite red-brown pigment, and franklinite (F) along ZnO (Z) in the case of Cr-franklinite ZnO decorated pigment (Figure 2). The microstructure of Pr-cerianite pigment is homogeneous, showing aggregates between 1–10 µm in size, integrated by homogeneous and finer particles of 0.5 µm in particle size (Figure 3); similarly, the Cr-franklinite powders show high homogeneity with aggregates between 0.5–3 µm, constituted by fine spherical particles of 0.3 µm of particle size. The SEM-EDX results in Figure 4 agree with the above observations, and all cation EDX signals are homogeneous in the corresponding composition mappings.

(c) As for the yellow pigments, the yttrium cerate $Y_2Ce_2O_7$ is the single crystalline phase (Y) detected by XRD (Figure 2). In the case of Ni,Sb-TiO_2 decorated rutile, only very weak peaks of residual $NiTiO_3$ (N) are detected accompanying the main rutile phase (R). Highly sintered particles 10–50 µm-sized are observed by SEM in the case of the yellow of Mo-yttrium cerate pigment (Figure 3), whereas in the case of Ni,Sb-rutile, the microstructure consists of aggregates between 1–5 µm-sized, integrated by finer spherical particles of 0.2–2 µm in particle size. The SEM-EDX results in Figure 4 correlate well with the above observations, since all cation EDX signals are homogeneous in the case of Mo-yttrium cerate yellow pigment, whereas the Ni $K_{\alpha1}$ signal show very scarce inhomogeneities associated with the presence of residual $NiTiO_3$ detected by XRD.

(d) Finally, concerning the studied black pigments, the hexagonal perovskite $Sr_4Mn_2CuO_9$ (S) is the only crystalline phase detected for the $Sr_4Mn_2CuO_9$ black-brown pigment (Figure 2). Co-chromite $CoCr_2O_4$ (C) and intense peaks of rutile (R) are detected in the case of $Co(Cr,Co)_2O_4$-decorated rutile black-green pigment. Regarding morphology, homogeneous microstructures are observed by SEM images (Figure 3) in both cases; the $Sr_4Mn_2CuO_9$ black-brown pigment consists of aggregates between 2–10 μm-sized integrated by fine spherical particles of 1 μm. In the case of the $Co(Cr,Co)_2O_4$-decorated rutile black-green pigment, fine aggregates between 1–5 μm-sized are observed with two kinds of particles: i.e., cubic particles of 1 μm and spherical particles of 0.2 μm. The SEM-EDX results in Figure 4 agree with the above observations, and all cation EDX signals are homogeneous in the case of $Sr_4Mn_2CuO_9$ black-brown pigment, whereas the Ti $K_{\alpha1}$ signal corroborates the presence of a rutile phase associated with the largest cubic particles (around 1 μm) observed in SEM images in the case of the $Co(Cr,Co)_2O_4$- rutile decorated black- green pigment.

4.2. UV-Vis-NIR Reflectance Spectra

The UV-Vis-NIR reflectance spectra of powders for both families of pigments are shown in Figure 5.
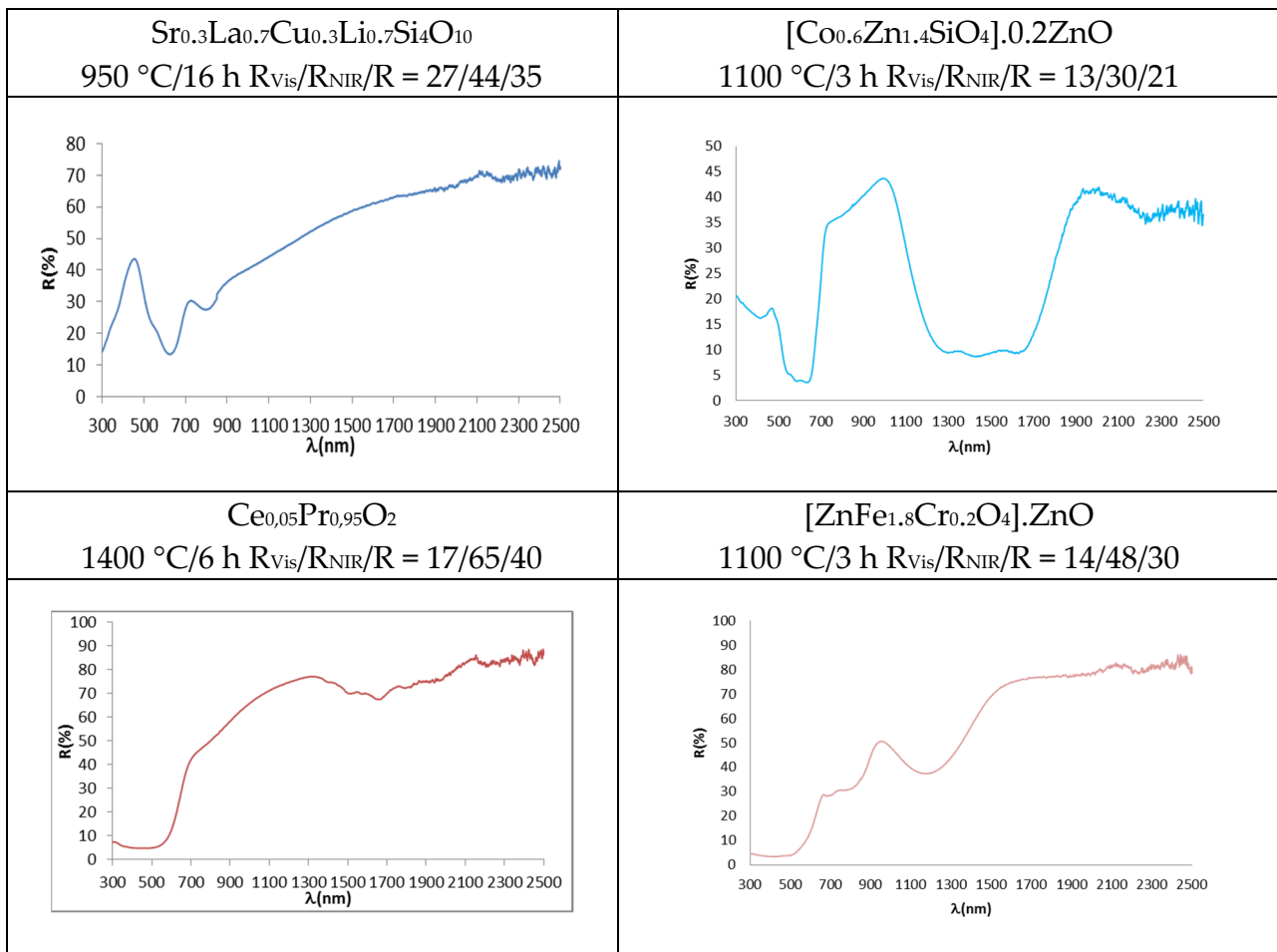
Figure 5. *Cont*.
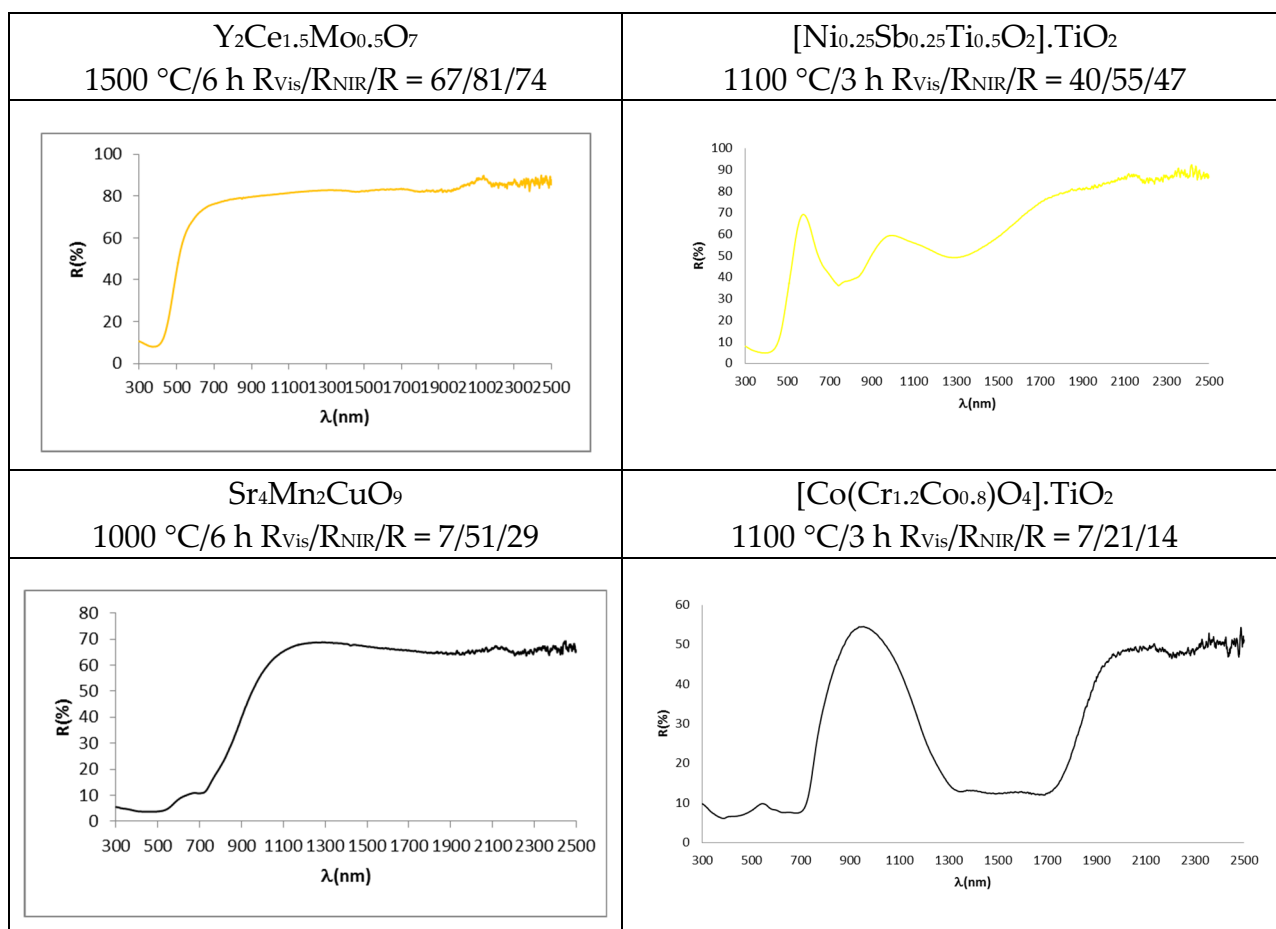
Figure 5. UV-Vis-NIR Reflectance spectra of powders of the both families of pigments.

(a) In the case of blue pigments, the structure of La,Li-SrCuSi$_4$O$_{10}$ wesselsite is composed of rings of four SiO$_4$ tetrahedra which are linked together by square-planar coordinated copper, thus forming double copper silicate layers which are joined by alkali-earth cations in a distorted cubic geometry. In the corresponding optical spectrum (Figure 5), three broad transitions are observed in the visible region originated from weakly-allowed d-d transitions of copper (despite a symmetry close to D$_{4h}$ at the copper centre) due to vibronic coupling. The three transitions, observed as minimums of reflectance, occur at 800 nm ($^2B_{1g} \rightarrow {}^2B_{2g}$), 630 nm ($^2B_{1g} \rightarrow {}^2E_g$) and 540 nm ($^2B_{1g} \rightarrow {}^2A_{1g}$) [32,33]. As for the classical Co-Zn$_2$SiO$_4$ willemite, its structure is an orthosilicate with all atoms in general position and composed of a framework of tetrahedra accommodating zinc and silicon in three different fourfold crystallographic sites; a deep blue colour is obtained by doping the willemite structure with cobalt, which replaces zinc ions in tetrahedral positions. The advantage of willemite pigments comes from the lower amount of Co needed to obtain suitably saturated blue hues with respect to spinel CoAl$_2$O$_4$ or olivine Co$_2$SiO$_4$; moreover, the use of an excess of ZnO protects the pigment from the attack of ZnO-rich glazes [44]. The blue colour is associated with Co^{2+} in tetrahedral coordination environment, which shows a strong absorbance with three bands at 540, 590 and 640 nm (for the colour) associated with the splitting of $^4A_2(F) \rightarrow {}^4T_1(P)$ transition due to the Jahn-Teller distortion. An additional strong and broad absorption appears at 1200–1600 nm (due to the coupling of $^4A_2(F) \rightarrow {}^4T_1(F)$ and $^4A_2(F) \rightarrow {}^4T_2(F)$ d-d transitions bands at 1400 nm and 1600 nm, respectively), which hinders NIR reflectance in this range [10,46].

(b) Regarding the red-brown pigments, it has been discussed above that Pr^{4+} doping in Pr-CeO$_2$ introduces an additional conduction band, and its associated charge transference band absorbs from 610 nm, showing a semiconductor feature with a band gap of 2.0 eV calculated using the Tauc procedure (direct semiconductor) (Figure 5) [18,19,43]. In the case of Cr-franklinite, Cr^{3+} enters, replacing Fe^{3+} in the normal spinel $ZnFe_2O_4$, and the following absorption bands are detected in the UV-Vis-NIR reflectance spectra of fired powders: (a) intense bands at 300–520 nm, (b) weak band centred at 680 nm, (c) medium band at 780 nm and (d) intense band at 1200 nm. It is difficult to distinguish between the presence of Cr^{3+} or Fe^{3+} ions in octahedral sites in the UV-Vis-NIR spectra of samples containing simultaneously both ions in these positions, because its bands are overlapped to a high extent. However, the main characteristic of Fe^{3+} ions in octahedral sites is the strong absorption associated with the transitions $^6A_{1g}(S) \rightarrow {}^4A_{1g}, {}^4E(G)$, which overlaps with the charge transference band at 400–500 nm that dominates the absorption spectrum of the powders, and the band gap associated to this charge transference band is 1.9 eV (Figure 5). The bands at around 770 and 1200 nm are typical characteristics of the zinc ferrite, which are attributed to $^6A_{1g}(S) \rightarrow {}^4T_{2g}(G)$ and $6A_{1g}(S) \rightarrow {}^4T_{1g}(S)$ for d-d electron transition of Fe^{3+} [47,48]. These Fe^{3+} bands overlap with those of Cr^{3+} in octahedral coordination, namely: (a) three main parity-forbidden transitions ($^4A_2(^4F) \rightarrow {}^4T_2(^4F)$ at 570 nm and $^4A_2(^4F) \rightarrow {}^4T_1(^4F)$ at 445 nm, which are partially overlapped, and $^4A_2(^4F) \rightarrow {}^4T_2(^4P)$ at 235 nm, which overlaps with Cr^{3+}-O^{2-} charge transfer), (b) two weak Cr^{3+} spin-forbidden transitions ($^4A_2(^4F) \rightarrow {}^2T_1(^2G)$ and $^4A_2(^4F) \rightarrow {}^2E(^2G)$ that overlap [49,50].

(c) As for the yellow pigments, in the case of Mo-Y$_2$Ce$_2$O$_7$ solid solutions, the doping of Mo^{6+} replacing Ce^{4+} in Y$_2$Ce$_2$O$_7$ needs the formation of cation vacancies (Y$_2$Mo$_x$Ce$_{2-x}$O$_{7+x}$) in order to satisfy the lattice charge balance [24]; Mo^{6+} doping introduces an additional conduction band and its associated charge transference band O_{2p}–Mo_{4d} absorbs from 505 nm (band gap 2.5 eV, Figure 5), inducing a yellow colour. All wavelengths above 505 nm are practically reflected. In the case of Ni,Sb-TiO$_2$ decorated rutile yellow pigment, the following spin-allowed bands of Ni^{2+} in octahedral coordination can be observed in Figure 5: $^3A_{2g}(^3F) \rightarrow {}^3T_{2g}(^3F)$ at 1200 nm, $^3A_{2g}(^3F) \rightarrow {}^3T_{1g}(^3F)$ at 800 nm (which overlaps with other spin-forbidden bands) and $^3A_{2g}(^3F) \rightarrow {}^3T_{1g}(^3P)$ at 450 nm (which overlaps with Ni^{2+}-O^{2-} band transfer with a band gap associated using the Tauc plot of 2.3 eV (direct type) [40,43].

(d) Concerning black pigments, in the case of the Sr$_4$Mn$_2$CuO$_9$ black-brown pigment, the broad optical absorption band at the shorter wavelength (400 nm) is attributed to the partial overlap of charge transfer transition and $^4A_{2g} \rightarrow {}^4T_{1g}$ d-d transition of Mn^{4+} in octahedral coordination (the band gap associated of this band is 1.2 eV, Figure 5). Weak transitions from weakly-allowed d-d transitions of copper, that fill the centre of the square faces of the trigonal prisms as described above, can be observed as minimums of reflectance at a at 800 nm ($^2B_{1g} \rightarrow {}^2B_{2g}$, very weak band), 715 nm ($^2B_{1g} \rightarrow {}^2E_g$) and 540 nm ($^2B_{1g} \rightarrow {}^2A_{1g}$) [32,33], but the band at 715 nm is associated by Bae at al. [37] to the $^2T_2 \rightarrow {}^2E$ transition of Cu^{2+} in a trigonally disordered tetrahedral crystal field [51]. In the case of the Co,Cr-decorated rutile black-green pigment, the absorption bands of Co^{2+} in tetrahedral coordination and Co^{2+} in octahedral coordination in the spinel are overlapped, and the following absorption bands are detected: a charge transfer band at 350 nm, a band at 450 nm (associated to $^4A_2(^4F) \rightarrow {}^4T_1(^4F)$ of Cr^{3+} in octahedral coordination), a strong absorbance with three bands at 540, 590 and 640 nm (associated to the splitting of $^4A_2(F) \rightarrow {}^4T_1(P)$ transition of Co^{2+} in tetrahedral coordination, due to Jahn-Teller distortion), and a strong absorption at a 1200–1600 nm range (due to the coupling of $^4A_2(F) \rightarrow {}^4T_1(F)$ and $^4A_2(F) \rightarrow {}^4T_2(F)$ d-d transitions bands in tetrahedral Co^{2+}) [46,49].

In order to know the effect of the dry powder coating (DPC) method over the synthesis of the powders, the four classic pigments were synthesized without the "core" of the pigment (ZnO or TiO$_2$) with stoichiometry Co$_{0.6}$Zn$_{1.4}$SiO$_4$, ZnFe$_{1.8}$Cr$_{0.2}$O$_4$ and Ni$_{0.25}$Sb$_{0.25}$Ti$_{0.5}$O$_2$, Co(Cr$_{1.2}$Co$_{0.8}$)O$_4$, respectively. The XRD of the stoichiometric samples (not shown) present the corresponding crystalline phases (willemite, franklinite, rutile and Co,Cr-spinel respectively) as single phases. The L*a*b* and R$_{NIR}$ of stoichiometric and DPC core shell powders and its applications in alkyd paint and double firing frit are shown in Table 1. It is observed that the values are very similar in powder and in alkyd paint or double firing frit, indicating that the decoration is effective and resists the attack of alkyd or the frit, however, the NIR reflectance of DPC samples show a slightly higher value (2–3%).

Table 1. L*a*b* and R$_{NIR}$ values of pigments with and without use of the dry powder coating (DPC) stoichiometry.

Stoichiometry	Powder	10 wt.% In Alkyd Paint	3 wt.% in Double Firing Frit
Co$_{0.6}$Zn$_{1.4}$SiO$_4$	L*a*b* = 28.0/−4.1/−26.0 R$_{NIR}$ = 27	L*a*b* = 45.2/−6.3/−16.2 R$_{NIR}$ = 38	L*a*b* = 54.2/−3.7/−23.0 R$_{NIR}$ = 52
[Co$_{0.6}$Zn$_{1.4}$SiO$_4$]·0.2ZnO	L*a*b* = 30.1/−3.8/−24.6 R$_{NIR}$ = 30	L*a*b* = 47.5/−6.2/−15.0 R$_{NIR}$ = 41	L*a*b* = 56.2/5.5/−21.1 R$_{NIR}$ = 53
ZnFe$_{1.8}$Cr$_{0.2}$O$_4$	L*a*b* = 33.1/22.6/19.0 R$_{NIR}$ = 46	L*a*b* = 37.1/20.0/18.0 R$_{NIR}$ = 50	L*a*b* = 46.1/17.9/19.0 R$_{NIR}$ = 55
[ZnFe$_{1.8}$Cr$_{0.2}$O$_4$]·ZnO	L*a*b* = 36.2/22.1/20.6 R$_{NIR}$ = 48	L*a*b* = 39.4/20.2/18.9 R$_{NIR}$ = 53	L*a*b* = 48.5/18.1/17.9 R$_{NIR}$ = 56
Ni$_{0.25}$Sb$_{0.25}$Ti$_{0.5}$O$_2$	L*a*b* = 85.0/−4.0/56.0 R$_{NIR}$ = 53	L*a*b* = 80.0/−4.0/50.4 R$_{NIR}$ = 64	L*a*b* = 87.9/−2/53.0 R$_{NIR}$ = 59
[Ni$_{0.25}$Sb$_{0.25}$Ti$_{0.5}$O$_2$]·TiO$_2$	L*a*b* = 84.3/−4.3/54.1 R$_{NIR}$ = 55	L*a*b* = 81.8/−4.4/48.0 R$_{NIR}$ = 70	L*a*b* = 78.7/−0.7/52.6 R$_{NIR}$ = 60
Co(Cr$_{1.2}$Co$_{0.8}$)O$_4$	L*a*b* = 47.6/−2.0/4.6 R$_{NIR}$ = 18	L*a*b* = 37.6/−2.3/3.6 R$_{NIR}$ = 26	L*a*b* = 50.6/−4.1/0.6 R$_{NIR}$ = 41
[Co(Cr$_{1.2}$Co$_{0.8}$)O$_4$]·TiO$_2$	L*a*b* = 49.3/−2.9/5.8 R$_{NIR}$ = 21	L*a*b* = 39.6/−3.4/4.3 R$_{NIR}$ = 28	L*a*b* = 51.4/−5.2/1.0 R$_{NIR}$ = 43

*4.3. Colour, Colorimetry (L*a*b* and C*h*) and Reflectance Parameters (R$_{Vis}$/R$_{NIR}$/R) of the Powders*

The image of the powders, showing its colour and its colorimetry (L*a*b* and C*h*) and reflectance parameters (R$_{Vis}$/R$_{NIR}$/R) are collected in Figure 6 and the results are discussed for each colour:

(a) As for blue pigments, the chroma C* is higher for the classical Co-willemite, and in both cases, it is very similar to its b* value. The lightness L* of the rare earth pigment is high and falls out of the Munsell blue range (L* = 25–35), but its R$_{NIR}$ is higher. For the comparison of the performance as cool pigments, CaCO$_3$ was added as binder to the pigments and the evolution of colorimetry and reflectance data are shown in Table 2; likewise, the representation of R$_{NIR}$ versus lightness L* of the blue pigments with gradual addition of the binder CaCO$_3$ is presented in Figure 7. According to Figure 7, it is observed that rare earths pigments always show higher L* and R$_{NIR}$ values, and the values of both pigments (classical and rare earth-based) follow a linear relationship (R^2 value > 0.92). Therefore, the normalized R$_{NIR}$30 value (reflectance associated to a L* = 30), which is proposed for blue hue evaluation, may be estimated as 30% for willemite and 7% for wesselsite blue. Thus, the blue Co-willemite powder shows better performance as a cool pigment.

$Sr_{0.3}La_{0.7}Cu_{0.3}Li_{0.7}Si_4O_{10}$ 950 °C/16 h	$Ce_{0.95}Pr_{0.05}O_2$ 1400 °C/6 h	$Y_2Ce_{1.5}Mo_{0.5}O_7$ 1500 °C/6 h	$Sr_4Mn_2CuO_9$ 1000 °C/6 h
L*a*b* = 62.3/−4.4/−19.9	50.6/17.5/12,8	85.2/0.2/45.3	43.9/7.2/6.3
C*h* = 20.4/257.5	21.7/36.2	45.3/89.8	9.6/41.2
$R_{Vis}/R_{NIR}/R$ = 27/44/35	17/65/40	67/81/74	7/51/29
$R_{NIR}30$ = 7	$R_{NIR}55$ = 69	$R_{NIR}85$ = 80	$R_{NIR}30$ = 50
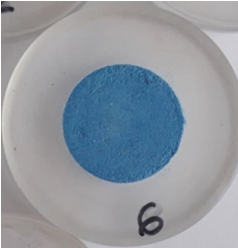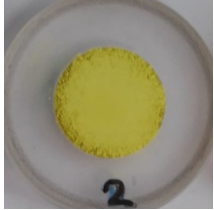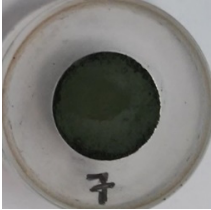
$[Co_{0.6}Zn_{1.4}SiO_4].0.2ZnO$ 1100 °C/3 h	$[ZnFe_{1.8}Cr_{0.2}O_4].ZnO$ 1100 °C/3 h	$[Ni_{0.25}Sb_{0.25}Ti_{0.5}O_2].TiO_2$ 1100 °C/3 h	$[Co(Cr_{1.2}Co_{0.8})O_4].TiO_2$ 1100 °C/3 h
L*a*b* = 30.1/−3.8/−24.6	36.2/22.1/20.6	84.3/−4.3/54.1	49.3/−2.9/5.8
C*h* = 24.9/261.2	30.2/43	54.3/94.5	6.5/116.6
$R_{Vis}/R_{NIR}/R$ = 13/30/21	14/48/30	40/55/47	7/21/14
$R_{NIR}30$ = 30	$R_{NIR}55$ = 59	$R_{NIR}85$ = 63	$R_{NIR}30$ = 13

Figure 6. Image of the powders, colour and its colorimetry (L*a*b* and C*h*) and reflectance parameters ($R_{Vis}/R_{NIR}/R$).

Table 2. Colorimetry and reflectance parameter for $CaCO_3$ addition to blue pigments.

$Sr_{0.3}La_{0.7}Cu_{0.3}Li_{0.7}Si_4O_{10}$ 950 °C/10 h	UV-Vis (%)	NIR (%)	TOTAL (%)	L a*b*
0% $CaCO_3$	26.6	44.3	35.2	62.3/−4.4/−19.9
20% $CaCO_3$	45.1	60.6	52.0	74.1/−5.1/−13.2
38.5% $CaCO_3$	53.9	66.0	59.3	79.6/−4.5/−8.4
50% $CaCO_3$	56.1	66.5	60.7	81.1/−4.1/−6.4
$[Co_{0.6}Zn_{1.4}SiO_4]\cdot0.2ZnO$ 1100 °C/3 h	UV-Vis (%)	NIR (%)	TOTAL (%)	L a*b*
0% $CaCO_3$	13.1	29.9	21.3	30.1/−3.8/−24.6
20% $CaCO_3$	17.9	33.8	24.6	49.7/−3.9/−14.7
38.5% $CaCO_3$	21.3	35.2	27.2	53.2/−4.3/−13.9
50% $CaCO_3$	24.2	37.5	29.8	56.4/−4.1/−13.1
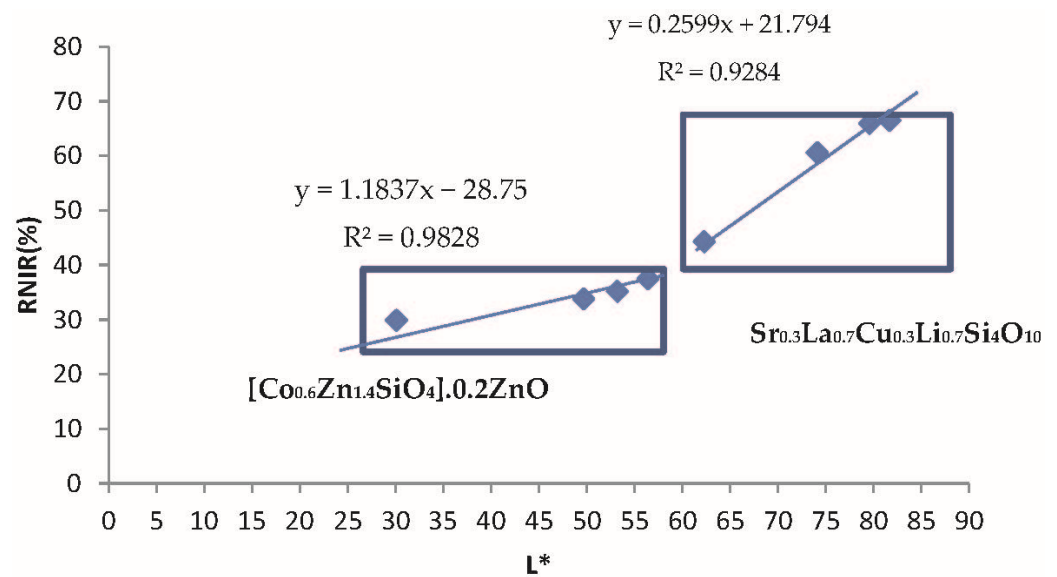
Figure 7. R_{NIR} versus lightness L* of blue pigments with gradual addition of the binder $CaCO_3$.

(b)   In the case of red-brown pigments, the chroma C* is higher for Cr-franklinite (C* = 30.2 vs. 21.7 for Pr-cerianite), being this value is closer to its absolute value of a*. The L* value is higher for Pr-cerianite (50.6 vs. 36.2 for Cr-franklinite) and shows higher R_{NIR} (65% vs. 48% for Cr-franklinite). The evolution of colorimetry and reflectance data with the gradual addition of $CaCO_3$ binder to the pigments are shown in Table 3 and the representation of R_{NIR} versus lightness L* follows a linear relationship in Figure 8. The $R_{NIR}55$ (reflectance associated to a L* = 55, considered for red hues) is 69% for rare-earth Pr-cerianite pigment and 59% for classical Cr-franklinite spinel pigment. Therefore red-brown Pr-cerianite powder shows better performance as a cool pigment.

Table 3. Colorimetry and reflectance parameters for $CaCO_3$ addition to red-brown pigments.

$Ce_{0.95}Pr_{0.05}O_2$ 1400 °C/6 h	UV-Vis (%)	NIR (%)	TOTAL (%)	L *a*b*
0% $CaCO_3$	17	65	40	50.6/17.5/12.8
20% $CaCO_3$	25.1	71.1	45.1	54.6/14.1/9.3
38.5% $CaCO_3$	30.1	70.0	47.4	60/13.3/9.0
50% $CaCO_3$	32.6	70.3	49.0	62.0/13.0/9.0
60% $CaCO_3$	37.9	73.1	53.1	61.7/11.7/8.1
80% $CaCO_3$	48.3	75.3	60.0	70.8/8.1/6.4
95% $CaCO_3$	63.8	80.0	70.7	81.1/4.4/5.6
100% $CaCO_3$	79.3	83.0	80.8	88.2/0.8/7.4
$[ZnFe_{1.8}Cr_{0.2}O_4]·ZnO$ 1100 °C/3 h	UV-Vis (%)	NIR (%)	TOTAL (%)	L*a*b*
0% $CaCO_3$	14.0	48.1	30.2	36.2/22.1/20.6
20% $CaCO_3$	18.2	46.0	29.7	41.5/19.0/12.6
38.5% $CaCO_3$	19.1	46.6	30.7	42.1/19.2/13.0
50% $CaCO_3$	19.8	47.7	31.9	45.2/18.7/10.1
60% $CaCO_3$	23.1	52.0	36.1	43.2/19.0/11.1
80% $CaCO_3$	29.2	56.1	43.0	48.1/17.2/12.5
100% $CaCO_3$	79.3	83.0	80.8	88.2/0.8/7.4
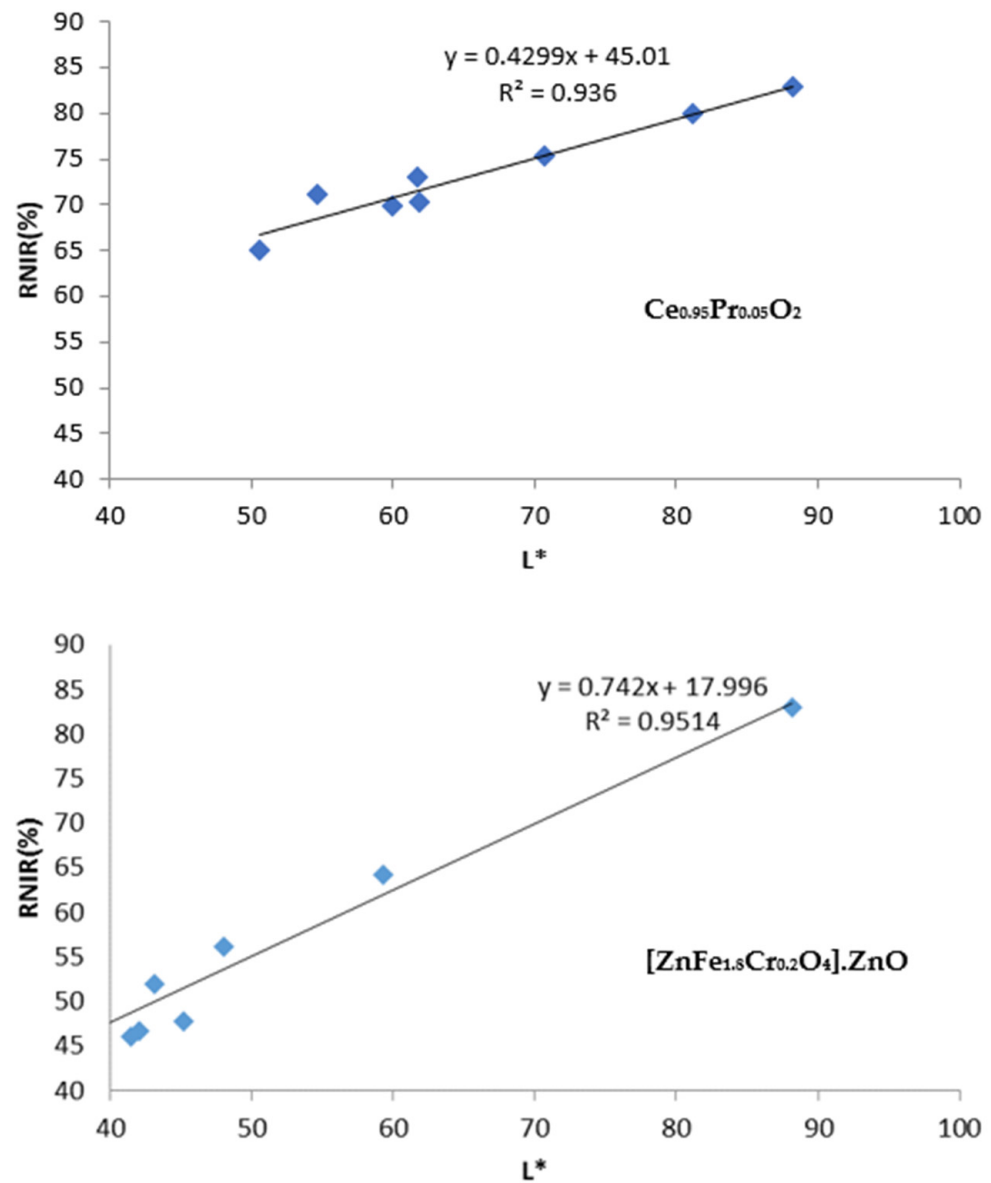
Figure 8. R_{NIR} versus lightness L^* of red-brown pigments with gradual addition of the binder $CaCO_3$.

(c) Regarding yellow pigments, the chroma C^* is higher for the Ni,Sb-rutile pigment ($C^* = 54.3$ vs. 45.3 for Mo-cerate pigment), and the lightness L^* is similar for both yellow pigments and included in the proposed yellow range ($L^* = 80$–90). The Mo-cerate yellow powder shows higher R_{NIR} (81% versus 55% for Ni,Sb-rutile). The evolution of colorimetry and reflectance data with the gradual addition of $CaCO_3$ binder to the pigments are shown in Table 4 and the representation of R_{NIR} versus lightness L^* follows a linear relationship in Figure 9. The $R_{NIR}85$ (reflectance associated to a $L^* = 85$, proposed for yellow hues) is 80% for the Mo-cerate pigment and 63% for classical Ni,Sb-TiO$_2$ decorated rutile pigment. Therefore Mo-cerate shows better performance as a cool pigment.

Table 4. Colorimetry and reflectance parameters for $CaCO_3$ addition to yellow pigments.

$Y_2Ce_{1.5}Mo_{0.5}O_7$ 1500 °C/6 h	UV-Vis (%)	NIR (%)	TOTAL (%)	L a*b*
0% $CaCO_3$	54.0	81.1	67.3	85.2/0.2/45.3
20% $CaCO_3$	66.7	80.4	72.20	87.13/−2.60/30.71
38.5% $CaCO_3$	68.11	82.7	74.40	87.56/−3.12/24.73
50% $CaCO_3$	67.26	87.0	75.76	88.8/−3.02/19.66
100% $CaCO_3$	79.26	82.92	80.83	88.23/0.83/7.37

$[Ni_{0.25}Sb_{0.25}Ti_{0.5}O_2]\cdot TiO_2$ 1100 °C/3 h	UV-Vis (%)	NIR (%)	TOTAL (%)	L a*b*
0% $CaCO_3$	39.6	54.7	47	84.28/−4.29/54.05
20% $CaCO_3$	44.11	57.9	50.23	84.1/−4.05/44.50
38.5% $CaCO_3$	45.59	58.6	51.36	84.2/−3.97/43.83
50% $CaCO_3$	46.90	59.5	52.48	84.4/−3.98/41.78
100% $CaCO_3$	79.3	83.0	80.8	88.2/0.8/7.4
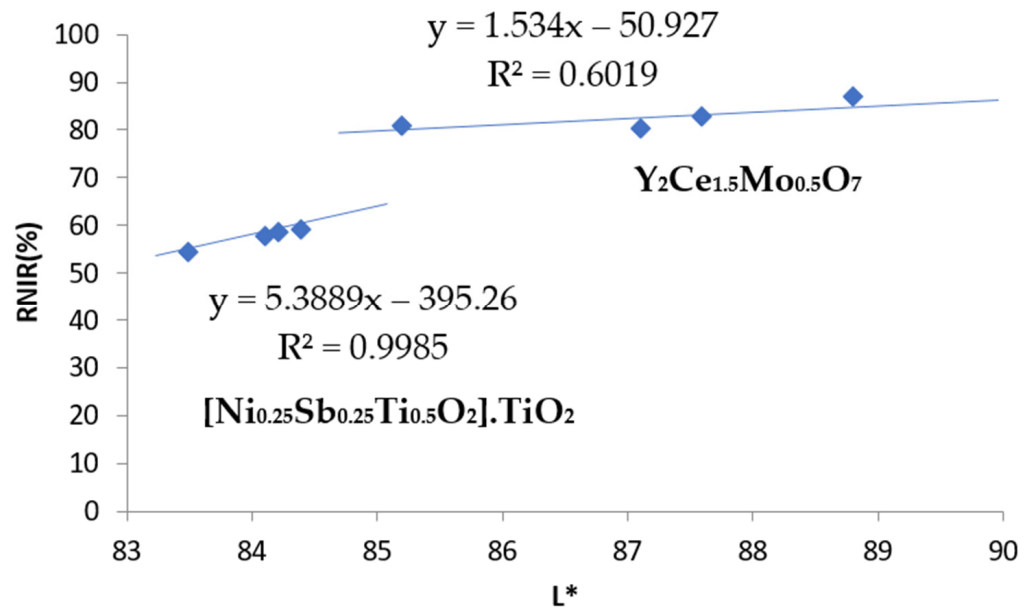
Figure 9. R_{NIR} versus lightness L* of yellow pigments with gradual addition of the binder $CaCO_3$.

(d) Concerning black pigments, from the data in Figure 6, the chroma C* is lower for chromite-rutile black-green (C* = 6.5 vs. 9.6 for Sr4Mn2CuO9), indicating a better black colour, and the hue is on the green range for this pigment (h* = 116.6), whereas the hue of black-brown Sr4Mn2CuO9 falls into the brown range (h* = 41.2). Lightness is low and similar for both dark pigments (44–50), although it is too high to be pure black pigment, since they do not enter into the range proposed above (L* = 30−0). Moreover, the Sr4Mn2CuO9 black-brown shows higher RNIR (51% versus 21% for chromite-rutile black-green). Finally, the evolution of colorimetry and reflectance data with the gradual addition of CaCO3 binder to the pigments are shown in Table 5, and the representation of RNIR versus lightness L* follows a linear relationship in Figure 10. The RNIR30 (reflectance associated to a L* = 30, considered for black hues) is 50% for Sr4Mn2CuO9 black-brown pigment and 13% for chromite-rutile black-green. Therefore, Sr4Mn2CuO9 shows better performance as cool pigment.

Table 5. Colorimetry and reflectance parameters for $CaCO_3$ addition to black pigments.

$Sr_4Mn_2CuO_9$ 1000 °C/6 h	UV-Vis (%)	NIR (%)	TOTAL (%)	L*a*b*
0% $CaCO_3$	7	50.9	28.5	43.91/7.15/6.29
20% $CaCO_3$	10.16	51.0	27.63	47.79/6.32/5.45
38.5% $CaCO_3$	12.38	51.1	28.83	50.57/5.98/5.08
50% $CaCO_3$	14.63	51.3	30.76	52.77/5.85/5.21
$[Co(Cr_{1.2}Co_{0.8})O_4] \cdot TiO_2$ 1100 °C/3 h	UV-Vis (%)	NIR (%)	TOTAL (%)	L*a*b*
0% $CaCO_3$	7	21	14	49.3/−2.9/5.8
20% $CaCO_3$	9	20	14.5	50.1/−2.5/5.0
38.5% $CaCO_3$	10	21	15.5	51.6/−2.3/4.9
50% $CaCO_3$	11	22	16.5	52.7/−2.2/4.1
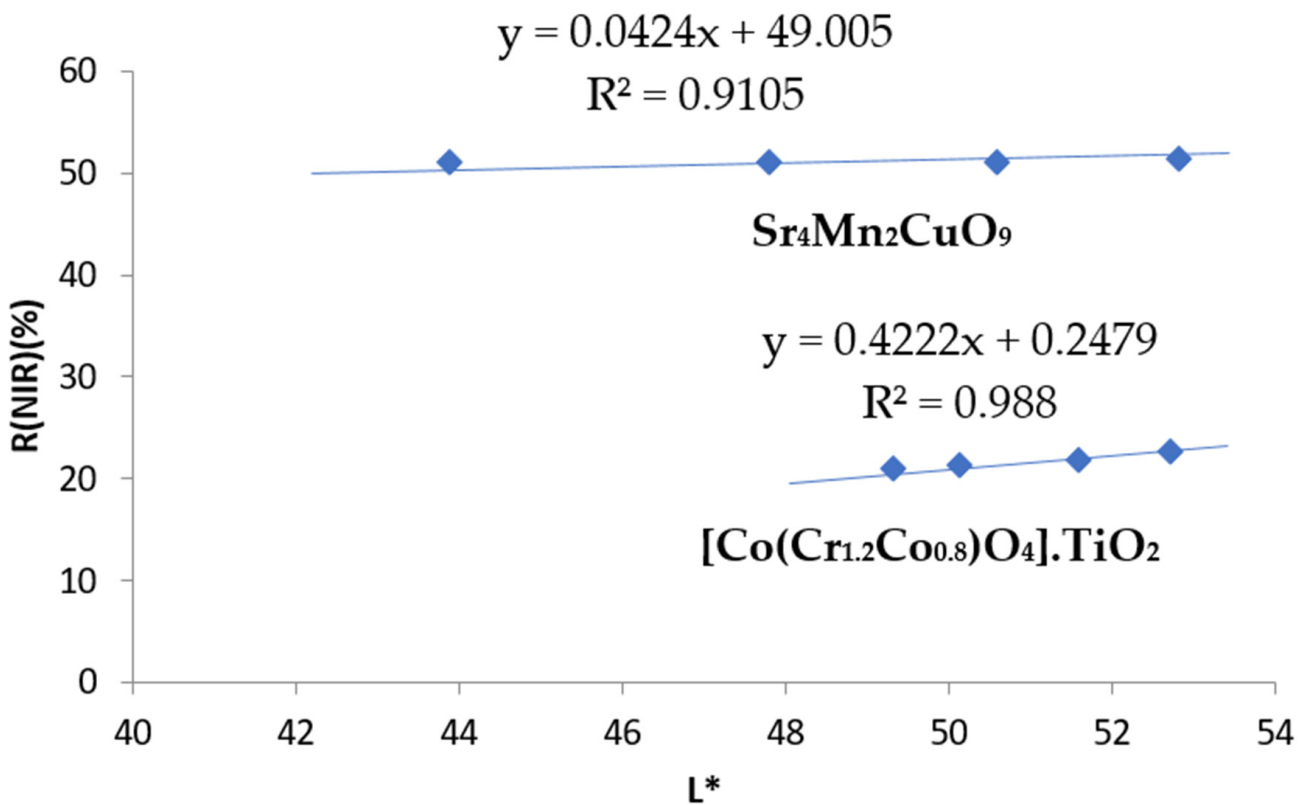
Figure 10. R_{NIR} versus lightness L* of black pigments with gradual addition of the binder $CaCO_3$.

4.4. Application of the Pigments: Stability and Colour Yield in Different Media

As above discussed, a pigment should be stable and exhibit an acceptable colorimetric performance when added (and thermally treated) to different media such as paints, glazes or ceramics. The colouring behaviour of the pigments was studied in three different matrices: (a) 10 wt.% in colourless alkyd paint, (b) 3 wt.% in a conventional lead-free double-firing frit of the SiO_2-CaO-ZnO system (1050 °C), and (c) 2% wt.% in porcelain powder (1190 °C).

The L*a*b* values of the different applications of the pigments are shown in Table 6, whereas its reflectance spectra and reflectance evaluation ($R_{Vis}/R_{NIR}/R$) are given in Figure 11 for rare earth pigments, and in Figure 12 for the classical cool pigments.

Table 6. L*a*b* values for the applications of pigments: (a) 10 wt.% in colourless alkyd paint, (b) 3 wt.% in double firing frit (1050 °C), (c) 2% wt.% in porcelain stoneware (1190 °C).

	$Sr_{0.3}La_{0.7}Cu_{0.3}Li_{0.7}Si_4O_{10}$ 950 °C/10 h	$Ce_{0.05}Pr_{0.95}O_2$ 1400 °C/6 h	$Y_2Ce_{1.5}Mo_{0.5}O_7$ 1500 °C/6 h	$Sr_4Mn_2CuO_9$ 1000 °C/6 h
(a)	72.4/−3.8/−3.0	51.6/19.9/15.5	81.3/0.4/18.9	46.6/7.8/7.5
(b)	80.5/−7.0/−5.6	65.6/18.2/20.0	87.6/−1.8/11.7	57.9/2.8/−0.2
(c)	76.8/1.2/9.8	70.3/6.8/11.4	79.2/1.5/11.5	73.4/1.7/11.6
	$[Co_{0.6}Zn_{1.4}SiO_4]\cdot 0.2ZnO$ 1100 °C/3 h	$[ZnFe_{1.8}Cr_{0.2}O_4]\cdot ZnO$ 1100 °C/3 h	$[Ni_{0.25}Sb_{0.25}Ti_{0.5}O_2]\cdot TiO_2$ 1100 °C/3 h	$[Co(Cr_{1.2}Co_{0.8})O_4]\cdot TiO_2$ 1100 °C/3 h
(a)	47.5/−6.2/−15.0	39.4/20.2/18.9	81.8/−4.4/48.0	39.6/−3.4/4.3
(b)	56.2/5.5/−21.1	48.5/18.1/17.9	78.7/−0.7/52.6	51.4/−5.2/1.0
(c)	64.8/−3.4/−13.1	46.3/3.4/4.7	79.0/−0.6/17.4	64.6/0.8/15.2
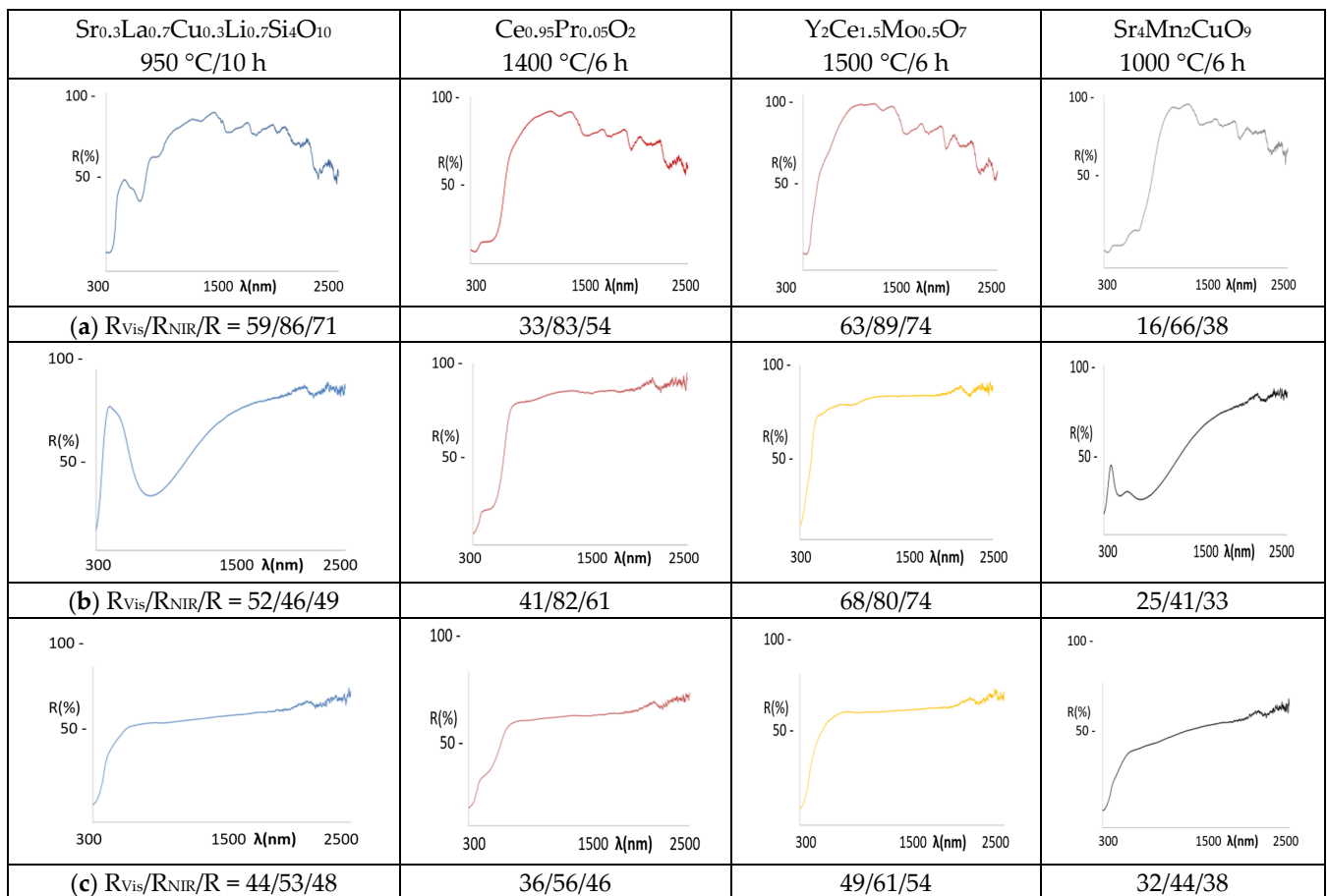
Figure 11. UV-Vis-NIR reflectance spectra of rare earth pigment applications: (**a**) 10 wt.% in colourless alkyd paint, (**b**) 3 wt.% in double firing frit (1000 °C), (**c**) 2% wt.% in porcelain powder (1190 °C).
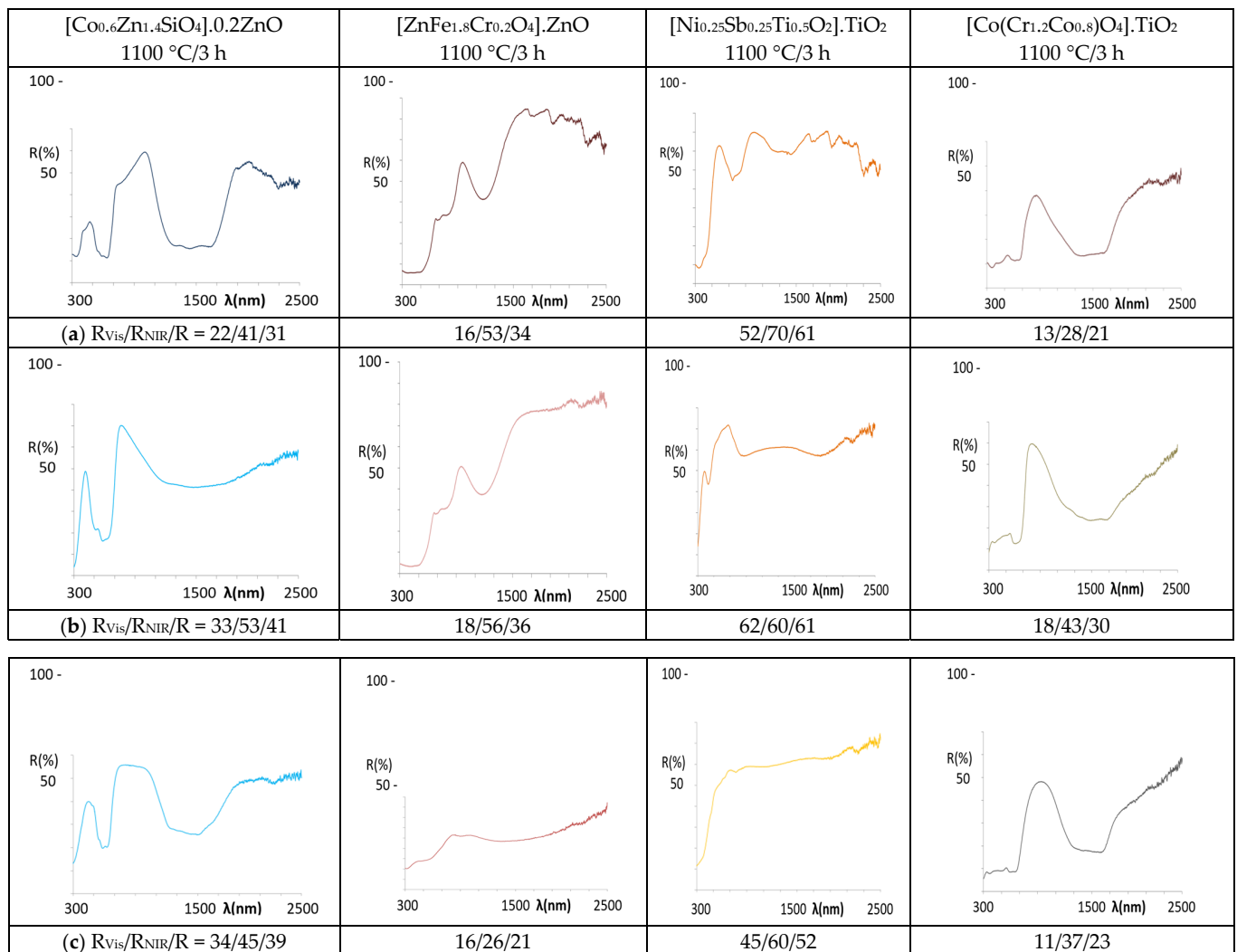
Figure 12. UV-Vis-NIR reflectance spectra of classical pigment applications: (**a**) 10 wt% in colourless alkyd paint, (**b**) 3 wt% in double firing frit (1050 °C), (**c**) 2% wt% in porcelain powder (1190 °C).

(a) As for the blue pigments, the application of La,Li-SrCuSi$_4$O$_{10}$ wesselsite develops pale blue hues in alkyd paint (b* = −3.0) and in double firing frit (b* = −5.6), but it is colourless in porcelain powder application. In agreement with the colour, the UV-Vis-NIR spectra of the applications (Figure 11) present similar features to the powder spectrum in the case of alkyd paint, indicating its stability in the paint. In the double firing frit application, only a strong absorption band centred at 750 nm is observed, which decreases the R$_{NIR}$ dramatically (46%, although its L* is only 80.5). This band is associated to Cu^{2+} ions dissolved in the alkaline glaze and located in high distorted octahedral sites (due to Jahn Teller distortion) [52], showing that the pigment is not stable in the glaze. Finally, no bands are detected in the application in porcelain powder, also indicating that the pigment is not stable in this medium. In the case of classical Co-willemite decorated ZnO, the blue colour is obtained in the three applications (Table 6) and the features of the spectra are similar in all cases (Figure 12), maintaining the spectrum of the powder, which is associated with tetrahedral Co^{2+}. Nevertheless, in the case of double firing frit, the absorption at 1200–1600 nm range (due to the coupling of $^4A_2(F) \rightarrow {}^4T_1(F)$ and $^4A_2(F) \rightarrow {}^4T_2(F)$) shows an unusual low intensity and the NIR reflectance increases in this application; this behaviour has been observed in nanopowders of rare earth doped cobalt aluminate [53]. Following

DCMA [3] classification, La,Li-SrCuSi$_4$O$_{10}$ wesselsite pigment belongs to Category B and Co-willemite decorated ZnO to Category A.

(b) In the case of red-brown pigments, the colour of Pr-cerianite is maintained in the three applications, with a* values around 19 in the alkyd paint and double firing frit, although in porcelain powder, a* value decreases to 6.8 (Table 6). The optical spectrum of the powder is maintained in all the applications (Figure 11), and only in alkyd paint the spectrum shows weak absorptions in the NIR range, which can be observed always associated with all the applications with the alkyd resin. Concerning the classical Cr-franklinite spinel pigment, the red-brown colour is maintained in the alkyd paint and in double firing frit (a* between 18 and 20), but it darkens in the porcelain powder application. The reflectance spectra of alkyd and double firing frit applications indicate the stability of the pigment (Figure 12), showing similar features to the powder spectrum; instead, the absorption bands observed at 300 and 500 nm produce the darkening of the sample for the porcelain powder application; moreover, a band at 900 nm and a strong absorption between 1200–1700 diminish the NIR reflectance of this application, probably associated to the decomposition of franklinite and partial reduction of iron (III) to iron (II). Therefore, both Pr-cerianite and Cr-franklinite spinel belongs to Category A but Cr-franklinite is unstable in porcelain powder.

(c) Regarding yellow pigments, the Mo-cerate yellow pigment loses the yellow hue (b* = 45.3 in powder, Figure 6) in the applications, and only in alkyd paint shows an indifferent b* = 18.9 (Table 6). The UV-Vis-NIR reflectance spectra of the applications (Figure 11) only indicate moderate absorption at 505 nm in the alkyd application, whereas in the case of double firing frit and porcelain powder, there is no evidence of absorption at 500 nm, indicating that the pigment is not stable in this medium. The Ni,Sb-rutile pigment, which shows b* = 54.1 in powder (Figure 6), maintains b* = 48 and L* = 81.8 in alkyd paint (into the range of high chromaticity for yellow), and even a higher b* (52.6) value in the double firing frit, but b* decreases to only 17.4 and L* to 79.0 (out of the range) for porcelain powder, indicates that the pigment is not stable and this application is colourless. The UV-Vis-NIR reflectance spectra of the applications (Figure 12) indicate similar features in the case of alkyd paint, whereas the spectrum is different for the double firing application, showing low absorption in the UV range and a broadening of the bands associated with Ni^{2+} in octahedral coordination. In the case of porcelain powder, no absorption bands are detected. From the proposed classification, Mo-cerate belongs to Category C and, considering the Zn rich glaze used in this study, Ni,Sb-rutile belongs to Category B of the pigments.

(d) Concerning the black pigments, the Sr$_4$Mn$_2$CuO$_9$ black-brown pigment maintains the colour in alkyd paint and double firing frit, whereas only a light darkening is observed in the case of porcelain powder. The corresponding UV-Vis-NIR reflectance spectrum of the applications (Figure 11) shows a similar spectrum to the powder in alkyd paint, whereas in the double firing application it shows a broadening of the absorption bands of Mn^{4+} in octahedral coordination and lower intensity of reflectance (particularly the band at 715 nm associated with $^4A_2(^4F) \rightarrow {}^4T_2(^4F)$ transition), which implies a decrease of reflectance in the 700–1000 nm, and thus decreasing its R$_{NIR}$ performance. As for the application in porcelain powder, only a light absorption in the 700–900 nm range is observed, indicating the low stability of the black-brown pigment in this medium. In the case of Co,Cr decorated rutile black-green pigment, the colour is maintained in all applications, with UV-Vis-NIR spectra similar to the powder spectrum, associated with Co^{2+} in tetrahedral coordination and Cr^{3+} in octahedral coordination; this confirms the stabilization of the pigment in the three applications, and show a R$_{NIR}$ higher than the powder. Therefore, both Sr$_4$Mn$_2$CuO$_9$ black-brown and Co,Cr decorated rutile black-green belong to Category A of pigments, however, Sr$_4$Mn$_2$CuO$_9$ black-brown is not stable in porcelain stoneware powder.

Finally, Table 7 summarizes the R_{NIR} values of the powders and its stable applications, along with its DCMA Category classification. In all applications, the NIR reflectance increases with respect to powder, especially in alkyd paint, but this increase, as it is discussed above, does not necessarily prove good performance as a cool pigment, because in some cases, the lightness and chroma of the colour is out of range, which is associated with pale colors and not with cool performance.

Table 7. R_{NIR} (%) of the powder and its stable applications along with its Category (ns = no stable).

	(A) Powder	(B) Alkyd Paint	(C) Double Firing Frit (1050 °C)	(D) Porcelain Stoneware (1190 °C)	Category
Blue					
$Sr_{0.3}La_{0.7}Cu_{0.3}Li_{0.7}Si_4O_{10}$ 950 °C/10 h	44	86	46	ns	B
$[Co_{0.6}Zn_{1.4}SiO_4]\cdot 0.2ZnO$ 1100 °C/3 h	30	41	53	45	A
Red-brown					
$Ce_{0.05}Pr_{0.95}O_2$ 1400 °C/6 h	65	83	82	56	A
$[ZnFe_{1.8}Cr_{0.2}O_4]\cdot ZnO$ 1100 °C/3 h	48	53	56	ns	A
Yellow					
$Y_2Ce_{1.5}Mo_{0.5}O_7$ 1500 °C/6 h	81	89	ns	ns	C
$[Ni_{0.25}Sb_{0.25}Ti_{0.5}O_2]\cdot TiO_2$ 1100 °C/3 h	55	70	60	ns	B
Black					
$Sr_4Mn_2CuO_9$ 1000 °C/6 h	51	66	41	ns	A
$[Co(Cr_{1.2}Co_{0.8})O_4]\cdot TiO_2$ 1100 °C/3 h	21	28	43	37	A

5. Conclusions

The high NIR reflectance of coloured powders is a necessary, but not sufficient, condition to be considered as a good performant of cool pigments. Usually, a satisfactory colour evaluation of coloured powders by a* or b* parameters, along with a high reflectance in the NIR range, measured by the UV-Vis-NIR (300–2500 nm) diffuse reflectance spectroscopy of powder, are considered as sufficient arguments to infer its good performance as cool pigments. However, this assumption may be erroneous sometimes, and a normalized solar reflectance to a given L* value should be adopted.

A palette of high NIR reflectance or cool ceramic pigments based on rare earths (except the black) were compared with a palette based on the coolest optimized traditional pigments obtained by the ceramic method. The rare earths (which lack of intense absorption bands in the NIR range and therefore show high R_{NIR} reflectance) were: (a) Blue of La,Li doped $SrCuSi_4O_{10}$ wesselsite, (b) Red-brown of Pr-CeO_2 cerianite, (c) Yellow of Mo-$Y_2Ce_2O_7$ yttrium cerate and (d) Black-brown of $Sr_4Mn_2CuO_9$ hexagonal perovskite).

The classical family studied were: (a') Blue of Co-Zn_2SiO_4 willemite (b') Red-brown of Cr-$ZnFe_2O_4$ franklinite, (c') Yellow of Ni,Sb-TiO_2-decorated TiO_2 and (d') Black-green of Co($Cr_{2-x}Co_x$)O_4. This palette ws obtained following a dry powder coating (DPC) procedure to obtain "core-shell" pigments with a core of high reflectance base (e.g., TiO_2, ZnO) coated by a shell of the corresponding pigment.

In the case of the blue pigments, although the R_{NIR} of the powders are 44% and 30% for La,Li-wesselsite and Co-willemite, respectively, by gradual addition of $CaCO_3$ as the binder, the normalized $R_{NIR}30$ (NIR reflectance for mixture L* = 30) are 7% and 30%, respectively, thus having an inverse result. Regarding red-brown pigments, Pr-cerianite shows a higher $R_{NIR}55$ (NIR reflectance for mixture L* = 55: 69% versus 59% for the classical Cr-franklinite spinel) but the difference is lower than for R_{NIR} direct measurements in powders (65% for Pr-cerianite and 48% for Cr-franklinite). In the case of yellows, the rare earth pigment based on Mo-$Y_2Ce_2O_7$ yttrium cerate shows higher $R_{NIR}85$ (80% versus 63% for the Yellow of Ni,Sb-TiO_2) but the difference is lower than for R_{NIR} direct measurements in powders (81% and 55% respectively). For black pigments, the black-brown $Sr_4Mn_2CuO_9$ shows higher normalized $R_{NIR}30$ (50%, and 13% for classical Co($Cr_{2-x}Co_x$)O_4@TiO_2), showing in this case that the difference is greater than for powder R_{NIR} values (51% and 21%), respectively.

The pigmenting behaviour and stability in different media is checked in order to evaluate the performance as cool pigments. Three applications of the pigments were carried out: in alkyd paint (10 wt.%), in double firing frit (3 wt.%, 1050 °C) and in porcelain powder (2 wt.%, 1190 °C). The results show that the stability of the non-classical cool pigments is lower than that of classical pigments except in the case of the Pr-cerianite red brown pigment.

Author Contributions: The individual contributions are provided by the following statements: Conceptualization, G.M.; methodology, G.M. and M.L.; software, J.A.B., G.M. and M.L.; validation, G.M. and M.L.; formal analysis, G.M.; investigation, J.A.B., G.M. and M.L.; resources, J.A.B. and G.M.; writing—original draft preparation, J.A.B., G.M. and M.L.; writing—review and editing, G.M. and M.L.; visualization, J.A.B. and G.M.; supervision, G.M.; project administration, G.M.; funding acquisition, J.A.B., G.M. and M.L. All authors have read and agreed to the published version of the manuscript.

Funding: This research was funded by Universitat Jaume I. The authors gratefully acknowledge the financial support of Universitat Jaume I (UJI-B2021-73 project).

Institutional Review Board Statement: Not applicable.

Informed Consent Statement: Not applicable.

Conflicts of Interest: The authors declare no conflict of interest.

References

1. CPMA. *Classification and Chemical Description of the Complex Inorganic Colour Pigments*, 4th ed.; Dry Colour Manufacturers Association: Alexandria, VA, USA, 2010.
2. Monrós, G. *Scheelite and Zircon: Brightness, Color and NIR Reflectance in Ceramics*; Nova Science Publishers: New York, NY, USA, 2021; ISBN 978-1-53619-332-9.
3. CIE Comission International de l´Eclairage. *Recommendations on Uniform Color Spaces, Colour Difference Equations, Psychometrics Colour Terms*; Bureau Central de la CIE: Paris, France, 1978.
4. Munsell, A.H. *Atlas of the Munsell Color System*; Wadsworth, Howland & Co., Inc.: Boston, MA, USA, 1915.
5. Briggs, D.J.C. The Dimensions of Colour. Available online: http://www.huevaluechroma.com/082.php (accessed on 14 September 2022).
6. ISO International Standard 105-J03. Part J03: Calculation of Color Differences. ISO International Standard: London, UK, 2009.
7. Hanrahan, P.; Kruger, W. SIGGRAPH'93. In Proceedings of the 20th Annual Conference on Computer Graphics and Interactive Techniques, Anaheim, CA, USA, 2–6 August 1993; pp. 165–174.
8. Hecht, H.G. The Interpretation of Diffuse Reflectance Spectra. *J. Res. Natl. Bur. Stand. Phys. Chem.* **1976**, *80*, 567–583. [CrossRef] [PubMed]
9. Kortüm, G. *Reflectance Spectroscopy, Principles, Methods, Applications*; Springer: Berlin/Heidelberg, Germany, 1969; ISBN 978-3-642-88071.

10. Llusar, M.; Bermejo, T.; Primo, J.E.; Gargori, C.; Esteve, V.; Monrós, G. Karrooite green pigments doped with Co and Zn: Synthesis, color properties and stability in ceramic glazes. *Ceram. Int.* **2017**, *12*, 9133–9144. [CrossRef]

11. ASTM C1371. Standard Test Method for Determination of Emittance of Materials Near Room Temperature Using Portable Emisometers. ASTM International: West Conshohocken, PA, USA, 2004.

12. Cerro, S.; Gargori, C.; Llusar, M.; Monrós, G. Orthorhombic (Fe$_2$TiO$_5$)-monoclinic (Cr$_2$TiO$_5$) solid solution series: Synthesis by gel routes, coloring and NIR reflectivity evaluation. *Ceram. Int.* **2018**, *44*, 13349–13359. [CrossRef]

13. Gargori, C.; Cerro, S.; Fas, N.; Llusar, M.; Monrós, G. Red-brown ceramic pigments based on chromium doped ferrian armalcolite, effect of mineralizers. *Ceram. Int.* **2017**, *43*, 5490–5497. [CrossRef]

14. Gargori, C.; Cerro, S.; Fas, N.; Llusar, M.; Monrós, G. Study of the photocatalytic activity and cool characteristics of a novel palette of pigments. *Bol. Soc. Esp. Ceram. Vidr.* **2017**, *56*, 166–176. [CrossRef]

15. Levinson, R.; Berdahl, P.; Akbari, H. Solar spectral optical properties of pigments–Part II: Survey of common colorants. *Sol. Energy Mater. Sol. Cells* **2005**, *89*, 351–389. [CrossRef]

16. Dieke, G.H. *Spectra and Energy Levels of Rare Earth Ions in Crystals*; Wiley–Interscience: New York, NY, USA, 1968.

17. Calbo, J.; Sorlí, S.; Llusar, M.; Tena, M.A.; Monrós, G. Minimisation of toxicity in nickel ferrite black pigment. *Br. Ceram. Trans.* **2003**, *103*, 3–9. [CrossRef]

18. Garcia, A.; Llusar, M.; Calbo, J.; Tena, M.A.; Monrós, G. Low-toxicity red ceramic pigments for porcelainised stoneware from lanthanide-cerianite solid solutions. *Green Chem.* **2001**, *3*, 238. [CrossRef]

19. LLusar, M.; Vitaskova, L.; Sucova, P.; Tena, M.A.; Badenes, J.A.; Monrós, G. Red ceramic pigments of terbium-doped ceria prepared through classical and non-conventional coprecipitation routes. *J. Eur. Ceram. Soc.* **2010**, *30*, 37–52. [CrossRef]

20. Smith, A.E.; Mizoguchi, H.; Delaney, K.; Spaldin, N.A.; Sleight, A.W.; Subramanian, M.A. Mn^{3+} in trigonal bipyramidal coordination: A new blue chromophore. *J. Am. Chem. Soc.* **2009**, *131*, 17084–17086. [CrossRef]

21. Oregon State University Materials with Trigonal Bipyramidal Coordination and Methods of Making the Same. US Patent 8.282.728 B2, 11 June 2009.

22. Sheethu, J.; Mundlapudi, L.R. Lanthanum strontium copper silicates as intense blue inorganic pigments with high near-infrared reflectance. *Dyes Pigm.* **2013**, *98*, 540–546. [CrossRef]

23. Zhang, Y.; Zhang, Y.; Zhao, X.; Zhang, Y. Sol–gel synthesis and properties of europium–strontium copper silicates blue pigments with high near-infrared reflectance. *Dyes Pigm.* **2016**, *131*, 154–159. [CrossRef]

24. Vishnu, V.S.; Reddy, M.L. Near-infrared reflecting inorganic pigments based on molybdenum and praseodymium doped yttrium cerate: Synthesis, characterization and optical properties. *Sol. Energy Mater Sol. Cells* **2011**, *95*, 2685–2692. [CrossRef]

25. Raj, A.K.; Rao, P.P.; Sameera, S.; Divya, S. Pigments based on terbium-doped yttrium cerate with high NIR reflectance for cool roof and surface coating applications. *Dyes Pigm.* **2015**, *22*, 116–125. [CrossRef]

26. Jovani, M.; Sanz, A.; Beltrán-Mir, H.; Cordoncillo, E. New red-shade environmental-friendly multifunctional pigment based on Tb and Fe doped Y$_2$Zr$_2$O$_7$ for ceramic applications and cool roof coatings. *Dyes Pigm.* **2016**, *133*, 33–40. [CrossRef]

27. Gargori, C.; Galindo, R.; Cerro, S.; García, A.; Llusar, M.; Monrós, G. Synthesis of a new Ca$_x$Y$_{2-x}$V$_x$Sn$_{2-x}$O$_7$ yellow pigment. *Phys. Procedia* **2010**, *8*, 84–87. [CrossRef]

28. Lili, L.; Aijun, H.; Mingquan, Y.; Zhao, Z. Synthesis and characterization of Al^{3+} doped LaFeO$_3$ compounds: A novel inorgànic pigments with high near-infrared reflectance. *Sol. Energy Mater Sol. Cells* **2015**, *132*, 377–384. [CrossRef]

29. Bae, B.; Wendusu; Tamura, S.; Imanaka, N. Novel environmentally friendly inorganic yellow pigments based on gehlenite-type structure. *Ceram. Int.* **2016**, *42*, 15104–15106. [CrossRef]

30. Schildhammer, D.; Fuhrmann, G.; Petschnig, L.; Weinberger, N.; Schottenberger, H.; Huppertz, H. Synthesis and characterization of a new high NIR reflective ytterbium molybdenum oxide and related doped pigments. *Dyes Pigm.* **2017**, *138*, 90–99. [CrossRef]

31. Kim, T.; Kim, S.; Lin, C.; Liu, R.; Chan, T.; Im, S. Melilite-type blue chromophores based on Mn^{3+} in a trigonal-bipyramidal coordination induced by interstitial oxygen. *J. Mater Chem.* **2013**, *37*, 5843–5848. [CrossRef]

32. Pozza, G.; Ajò, D.; Chiari, G.; De Zuane, F.; Favaro, M. Photoluminescence of the inorganic pigments Egyptian blue, Han blue and Han purple. *J. Cult. Heritage* **2000**, *1*, 393–398. [CrossRef]

33. Kendrick, E.; Kirk, C.J.; Dann, C.J.S.E. Structure and color properties in the Egyptian Blue Family, M$_{1-x}$M'$_x$CuSi$_4$O$_{10}$, as a function of M, M' where M, M' = Ca, Sr and Ba. *Dyes Pigm.* **2007**, *73*, 13–18. [CrossRef]

34. Seitz, G.; Penin, N.; Decoux, L.; Wattiaux, A.; Duttine, M.; Gaudon, M. Near the Ferric Pseudobrookite Composition (Fe$_2$TiO$_5$). *Inorg. Chem.* **2016**, *55*, 2499–2507. [CrossRef] [PubMed]

35. Pfeffer, R.; Dave, R.N.; Dongguang, W.; Ramlakhan, M. Synthesis of engineered particulates with tailored properties using dry particle coating. *Powder Technol.* **2001**, *117*, 40–67. [CrossRef]

36. Ouabbas, Y.; Chamayou, A.; Galet, L.; Baron, M.; Thomas, G.; Grosseau, P.; Guilhot, B. Surface modification of silica particles by dry coating: Characterization and powder ageing. *Powder Technol.* **2009**, *190*, 200–209. [CrossRef]

37. Bae, B.; Takeuchi, N.; Tamura, S.; Imanaka, N. Environmentally friendly orange pigments based on hexagonal perovskite-type compounds and their high NIR reflectivity. *Dyes Pigm.* **2017**, *147*, 523–528. [CrossRef]

38. Ozel, E.; Yurdakula, H.; Turana, S.; Ardit, M.; Cruciani, G.; Dondi, M. Co-doped willemite ceramic pigments: Technological behaviour, crystal structure and optical properties. *J. Eur. Ceram. Soc.* **2010**, *30*, 3319–3329. [CrossRef]

39. Benda, P.; Kalendová, A. Anticorrosion properties of pigments based on ferrite coated zinc particles. *Phys. Procedia* **2013**, *44*, 185–194. [CrossRef]

40. Sorlí, S.; Tena, M.A.; Badenes, J.A.; Llusar, M.; Monrós, G. Study of nickel precursors in (Ni,M,Ti)O$_2$ (M = Sb, Nb) yellow ceramic pigments. *Br. Ceram. Trans.* **2004**, *103*, 10–14. [CrossRef]

41. Eliziárioa, S.A.; De Andrade, J.M.; Limac, S.J.G.; Paskocimas, C.A.; Soledade, L.E.B.; Hammer, P.; Longo, E.; Souza, A.G.; Santos, I.M.G. Black and green pigments based on chromium–cobalt spinels. *Mater. Chem. Phys.* **2011**, *129*, 619–624. [CrossRef]

42. Pu, Y.; Wang, G.; Chang, K.; Ling, Y.; Lin, Y.; Fitzmorris, B.C.; Liu, C.; Lu, X.; Tong, Y.; Zhang, J.Z.; et al. Au Nanostructure-Decorated TiO$_2$ Nanowires Exhibiting Photoactivity Across Entire UV-visible Region for Photoelectrochemical Water Splitting. *Nano Lett.* **2013**, *13*, 3817–3823. [CrossRef] [PubMed]

43. Tauc, J.; Grigorovici, R.; Vancu, A. Optical Properties and Electronic Structure of Amorphous Germanium. *Phys. Tatus Solidi* **1966**, *15*, 627–637. [CrossRef]

44. Schabbacha, L.M.; Marinoski, D.L.; Güthsb, S.; Bernardinc, A.M.; Fredel, M.C. Pigmented glazed ceramic roof tiles in Brazil: Thermal and optical properties related to solar reflectance index. *Solar Energy* **2018**, *159*, 113–124. [CrossRef]

45. Gaffey, S.J. Spectral reflectance of-carbonate minerals in the visible and near infrared (0.35-2.55 microns): Calcite, aragonite, and dolomite. *Am. Mineral.* **1986**, *71*, 151–162. [CrossRef]

46. Forés, A.; Llusar, M.; Badenes, J.A.; Calbo, J.; Tena, M.A.; Monrós, G. Cobalt minimisation in willemite (Co$_x$Zn$_{2-x}$SiO$_4$) ceramic pigments. *Green Chem.* **2000**, *2*, 93–100. [CrossRef]

47. Suwan, M.; Sangwong, N.; Supothina, S. Effect of Co and Pr doping on the properties of solar reflective ZnFe$_2$O$_4$ dark pigment. *IOP Conf. Ser. Mater. Sci. Eng.* **2017**, *182*, 012003. [CrossRef]

48. Pailhé, N.; Wattiaux, A.; Gaudon, M.; Demourges, A. Correlation between structural features and vis-NIR spectra of -Fe2O3 hematite an AFe$_2$O$_4$ spinel oxides (A = Mg, Zn). *J. Solid State Chem.* **2018**, *181*, 1040–1047. [CrossRef]

49. Dondi, M.; Matteucci, F.; Cruciani, G.; Gasparoto, G.; Tobaldi, D.M. Pseudobrookite ceramic pigments: Crystal structural, optical and technological properties. *Solid State Sci.* **2007**, *9*, 362–369. [CrossRef]

50. Prim, S.R.; García, A.; Galindo, R.; Cerro, S.; Llusar, M.; Folgueras, M.V.; Monrós, G. Pink ceramic pigment based on chromium doped M(Al$_{2-x}$Cr$_x$)O$_4$, M=Mg, Zn, normal spinel. *Ceram. Int.* **2013**, *39*, 6981–6989. [CrossRef]

51. Katiyar, R.S.; Kousik, S. Structural and optical properties of Zn$_{1-x}$Cu$_x$O thin films. In *Handbook of Zinc Oxide and Related Materials*; Feng, Z.C., Ed.; CRC Press: Boca Raton, FL, USA, 2013; Volume 1.

52. Monrós, G. Sol-Gel Materials for Pigments and Ceramics. In *The Sol-Gel Handbook—Synthesis, Characterization and Applications*; Levy, D., Zayat, M., Eds.; Wiley: Hoboken, NJ, USA, 2015; Volume 3, pp. 1145–1173. ISBN 9783527334865.

53. Tong, Y.; Zhang, H.; Wang, S.; Chen, Z.; Bian, B. Highly Dispersed Re-Doped CoAl$_2$O$_4$ Nanopigments: Synthesis and Chromatic Properties. *J. Nanomater.* **2016**, *2016*, 4169673. [CrossRef]